Marine and Petroleum Geology 153 (2023) 106284

Contents lists available at ScienceDirect

Marine and Petroleum Geology

journal homepage: www.elsevier.com/locate/marpetgeo

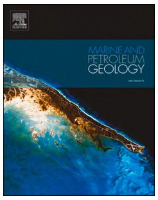

Evidence of deep fluid activity in Jurassic tight sandstone reservoirs in the Northern Kuqa Depression

Yifan Zhang[a], Kelai Xi[a,*], Yingchang Cao[a,b,**], Xianzhang Yang[c], Zhenping Xu[c], Lu Zhou[c], Guoding Yu[a], Zhanghua Han[a], Zehan Zhang[a]

[a] School of Geosciences, China University of Petroleum, Qingdao, Shandong, 266580, China
[b] Laboratory for Marine Mineral Resources, Qingdao National Laboratory for Marine Science and Technology, Qingdao, 266071, China
[c] Research Institute of Exploration and Development Petrochina Tarim Oilfield Company, Korla, 841000, China

ARTICLE INFO

Keywords:
Deep fluid
Authigenic quartz
Calcite
Diagenesis
Ahe formation
Kuqa depress
Tarim basin

ABSTRACT

Understanding diagenetic fluid types and their effects on diagenesis is important to identify the main control factors of reservoir characteristics and predict reservoir sweet spots. Reservoir space destruction caused by strong cementation is notable in the Lower Jurassic Ahe Formation sandstones near the deep-rooted fault (Yiqikelike Fault) in the Kuqa depression. Different authigenic minerals and widely varying cementation contents indicate the complexity of diagenetic fluids. Therefore, we investigated strong cementation using petrographic and geochemical methods, including cathodoluminescence, scanning electron microscopy, laser ablation inductively coupled plasma mass spectrometry, and stable isotope analysis. The contents of authigenic quartz and calcite increased as they approached the deep-rooted fault, with maximum concentration of quartz and calcite of up to 8.73% and 8.92%, respectively. Abnormally high homogenization temperatures of the fluid inclusions were observed in the quartz overgrowth, one of which reached 156 °C. In calcite, the rare earth element Eu exhibited abnormal characteristics, and the carbon isotopes ranged from −8.00‰ to −2.00‰. Therefore, it is likely that deep fluids are involved in reservoir diagenesis near a deep-rooted fault. This study provides a good example of diagenetic evolution in deep sandstone reservoirs and the negative effects of the involvement of deep fluids in diagenetic processes.

1. Introduction

The distinctive feature of the diagenesis of dense sandstone reservoir is the gradual reduction of sandstone pore volume with the continuation of buried diagenesis based on the original sedimentary configuration. Authigenic cementation is one of the main diagenetic effects controlling pore volume change (Liu and Zhang, 1992; Li et al., 2013). During the initial densification process of linear contact or concave–convex contact of sandstone clastic particles caused by compaction (Shou et al., 2004), the precipitation of additional authigenic minerals also densified the sandstone reservoir. Regarding cementation diagenesis in sandstone reservoirs, the relationship between diagenetic fluids and cementation in terms of the properties and evolution of diagenetic fluids has been studied (Wang et al., 1999; Zhu et al., 2008).

Factors affecting the diagenesis of sandstone reservoirs are closely related to the type and activity of diagenetic fluids (Schmidt and McDonald, 1982). The fluids affecting the reservoir can be divided into organic and carbon acids (Surdam et al., 1984; Ramm, 1992), atmospheric freshwater (Ehrenberg, 1993; Anna et al., 2009), deep fluids (Liu et al., 2011; Long et al., 2014; Su et al., 2016), formation water, and hydrocarbons. Therefore, clarifying the geological history of rock-forming fluids, type and time of rock-forming fluids with scale activity, and stratigraphic location where rock-forming fluids act is crucial to understand the genesis of dense reservoirs.

Four geothermal events in the Tarim Basin occurred during the Sinian-Cambrian, Ordovician, Early Permian, and Cretaceous, respectively (Chen et al., 1997). In the Late Cretaceous, the Kuqa depression experienced uplift in some areas, and the Yiqikelike and Tugerming areas formed the prototype of an anticline under the influence of horizontal compression, such as the Yiqikelike fault (Lu et al., 2000; Sun et al., 2009; Tao et al., 2014). The evolution of the Yiqikelike fault (Jia and Li, 2008; Shang et al., 2012; Huang and Wang, 2016; Pang et al.,

---

* Corresponding author.
** Corresponding author. School of Geosciences, China University of Petroleum, Qingdao, Shandong, 266580, China.
E-mail addresses: kelai06016202@163.com (K. Xi), cyc8391680@163.com (Y. Cao).

https://doi.org/10.1016/j.marpetgeo.2023.106284
Received 21 March 2023; Received in revised form 17 April 2023; Accepted 20 April 2023

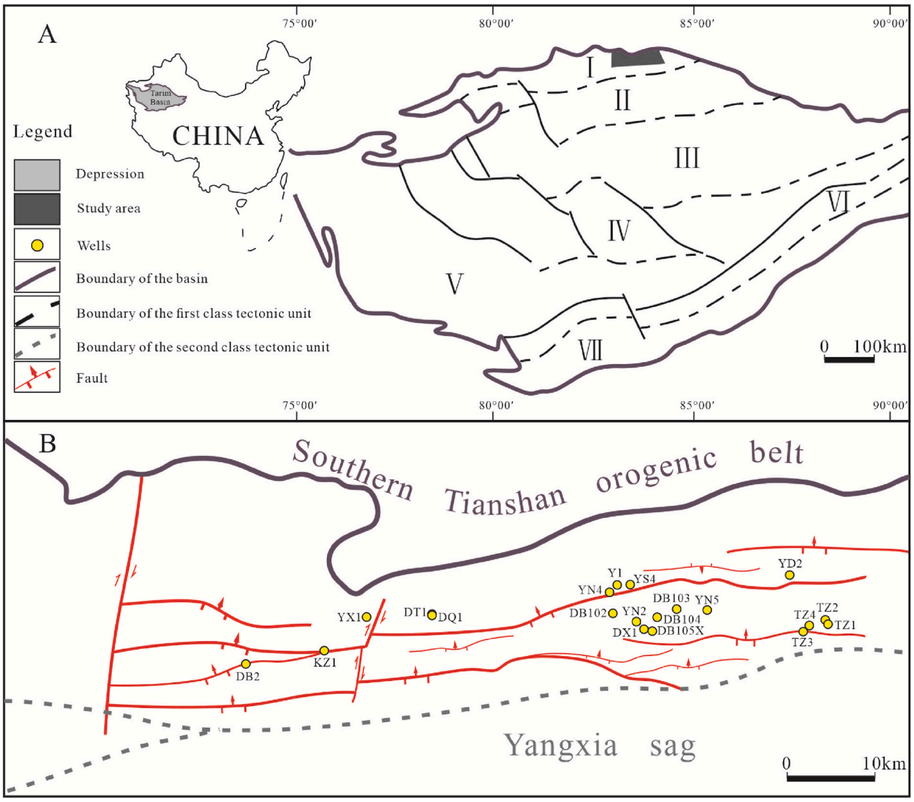

Fig. 1. (A) Location map of the study area and sub-tectonic units of the Tarim Basin (from Wang et al., 2009). (I) Kuqa Depression, (II) Tabei Uplift Zone, (III) Northern Depression Zone, (IV) Central Uplift Zone, (V) Southwestern Depression Zone, (Vi) Tanan Uplift Zone, (VII) Southeastern Depression Zone; (B) The study area and well locations.

2021) is well studied; it is a multi-stage active fault, which started in the Cretaceous, was active again after the Paleogene deposition, and remains active to this day. The strong activity of the Yiqikelike fault during the Miocene is crucial, it directly penetrated all the formations, which is required for the communication of deep fluids. The Yiqikelike fault evolution completely illustrates the possibility of deep fluids during the diagenetic evolution in this area. Therefore, it is important to determine how deep fluids were involved in diagenesis and the manner in which they acted and affected reservoir properties.

Deep fluid can be transported upward into the upper stratum through channels such as deep-rooted faults, in which SiO_2 crystallizes to form siliceous cements such as quartz overgrowth (Li et al., 2015). Additionally, the $CaCO_3$ precipitation from deep CO_2-rich fluid occurs at shallow depths (Duan and Li, 2008; Zhu et al., 2012). Silica and carbonate cement are the most common cement types in clastic reservoirs and significant authigenic minerals during diagenesis. The diagenetic fluid interactions related to siliceous and carbonate cement cause manifest changes in reservoir porosity and permeability, indicating that cementation has an important influence on reservoir properties and is of great significance to the reservoir performance of oil and gas.

The Kuqa depression is rich in natural gas resources and presents an important natural gas-producing area in the Tarim Basin (R. Zhang et al., 2014; Wang et al., 2016; Guo et al., 2016; Lai et al., 2017; Lu et al., 2018; Jiang and Sun, 2018; Tian et al., 2020). The wells YN2, YN5, and DB102 on the flank of the Yiqikelike backslope acquired industrial oil and gas flow (Wang and Long, 2010; Li et al., 2015), whereas the wells YS4 and YN4 in the back-slope axis only possessed oil and gas, without industrial gas flow (Yuan et al., 2014). In addition, diagenesis varies substantially from one structural style to another. The types of sandstone diagenesis in the Ahe Formation in the Yinan and Yishen areas are different. The kaolinite content of the Ahe Formation sandstones in the Yishen areas (wells YS4 and YN4) was higher than that in the Yinan areas (wells DB102 and YN2) (Ni et al., 2022). The closer to the Yiqikelike deep-rooted fault, the higher the kaolinite content in the sandstones of the Ahe Formation. The objectives of this study entailed (1) clarifying whether deep fluids are related to the strong cementation characteristics of authigenic quartz and calcite, and (2) analyzing the differences in reservoir quality at different structural styles owing to deep fluid influences.

2. Geological setting

The Kuqa depression is located in the northern Tarim Basin and extends to the South Tianshan Mountains to the north and the Tabei Uplift to the south (Wang and Long, 2010) (Fig. 1A). Since the Mesozoic, the Kuqa depression has experienced two major tectonic movements in the Late Mesozoic and Neogene periods (Li et al., 2005; Zeng et al., 2010), which were affected by the collision between the Indian plate and Lhasa block, and the Indian and Eurasian plates, respectively (X. Li et al., 2004). In the Late Cretaceous, the Kuqa depression experienced uplift in some areas, and the Yiqikelike and Tugerming areas formed the prototype of an anticline under horizontal compression. Since the Miocene, tectonic deformation started from north to south (Jia, 1999; Gong et al., 2015). The time of the emplacement of the thrust faults in the Yiqikelike and Kelasu anticlines ranged from the Kangcun to Xiyu stage with the formation of fault-related folds in turn (Liu et al., 2001; Zhang et al., 2003; Z. Li et al., 2004; Zeng, 2004). The Dibei area is located in the eastern part of the Yiqikelike tectonic zone of the Kuqa depression (Fig. 1A), which has experienced multiple phases of tectonic movements, leading to strong deformation and more developed retrograde fractures. The Dibei area is controlled by the Yiqikelike fault, which is a north-dipping, nearly east–west trending retrograde deep-rooted fault. The study area is located in the footwall of the Yiqikelike fault (Liu et al., 2004; Jiang et al., 2015).

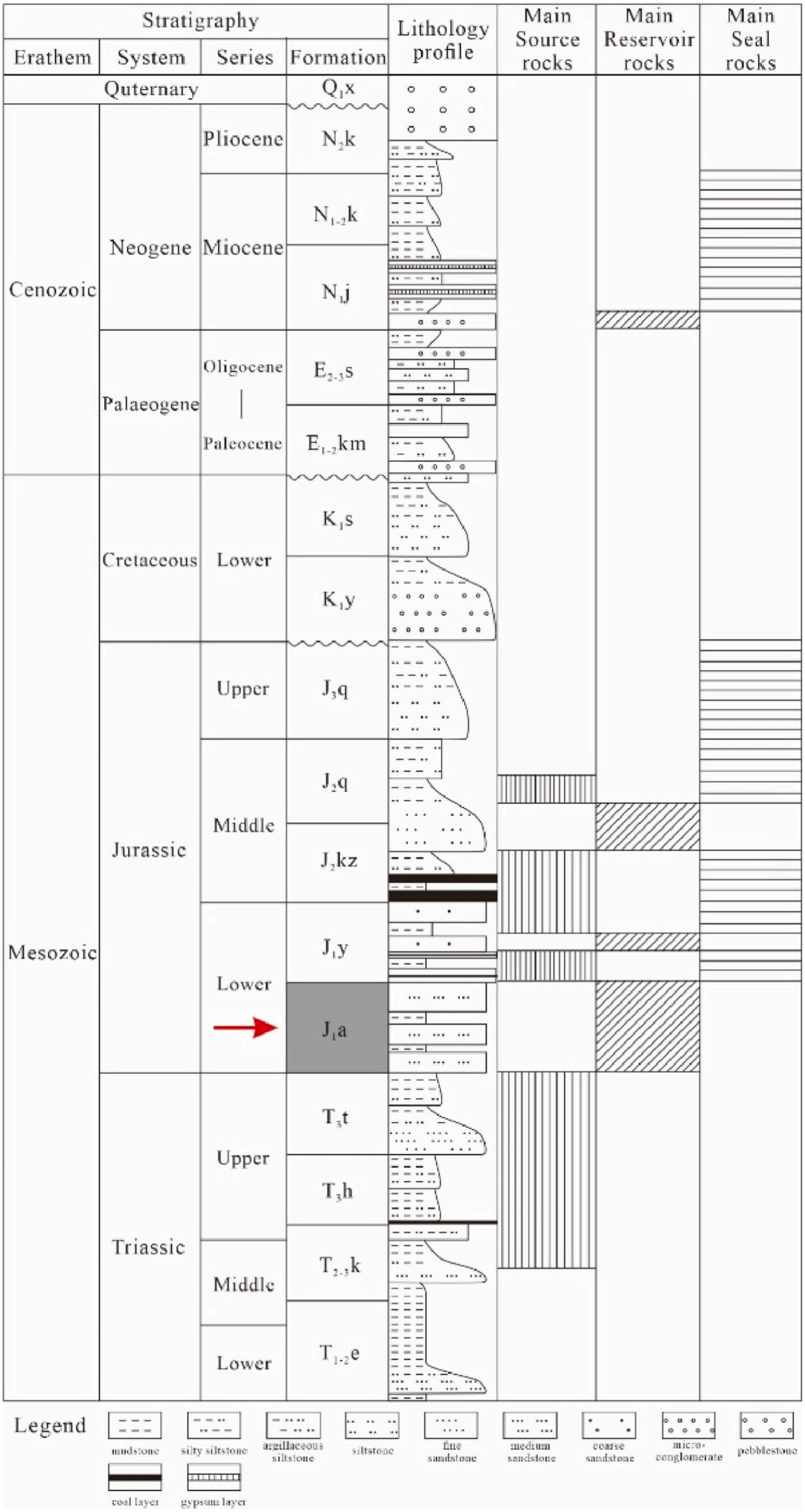

Fig. 2. Generalized Mesozoic-Quaternary stratigraphy of the Tarim Basin, showing major oil and gas combinations.

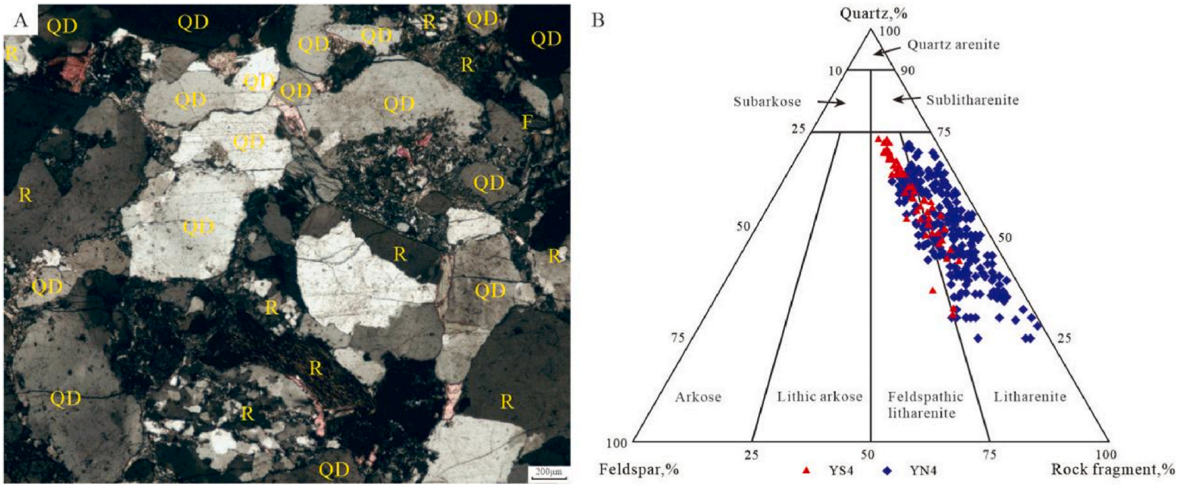

Fig. 3. Rock composition of the YS4 tight sandstone reservoirs: (A) Micrograph of thin section showing quartz, feldspar and rock fragments; (B) Classification of sandstone using Folk's (1974) classification.
QD—detrital quartz; F—feldspar; R—rock fragment.

The Lower Jurassic Ahe Formation in the northern tectonic zone is a set of braided river deltaic plain subphase sediments with grayish-white (gravelly) coarse sandstone, medium sandstone, and fine sandstone interbedded with thinly laminated conglomerate, sand conglomerate, and mudstone, with a thickness of 250–430 m. From top to bottom, it can be divided into a section of the Ahe Group (sand conglomerate with mudstone section), Ahe Group II (upper sand conglomerate section), and Ahe Group III (lower sand conglomerate section). Overall, the sandstones of the Ahe Group were developed with a thickness of 150–200 m and stacked and distributed in succession with a burial depth of 1200–8500 m. The Middle-Upper Triassic and Middle-Lower Jurassic coal-derived hydrocarbon source rocks are the main hydrocarbon source rocks of the Dibei gas reservoir (Tang et al., 2021; Jiang et al., 2021). The Triassic Huangshanjie Formation and Talicike Formation are oil layers, Jurassic Ahe Formation conglomerate is a reservoir, and Yangxia Formation coal measures the stratum as caprock. The sandstone reservoir is sandwiched between two sets of coal-derived hydrocarbon rocks, forming a "sandwich" structure of the source and reservoir symbiosis structure (Wang et al., 2022) (Fig. 2).

3. Methodology

3.1. Petrographic analysis

Thin sections (118) from sandstone core plugs selected from two wells near the deep-rooted fault were petrographically analyzed. The samples were impregnated with blue resin before thin sectioning to highlight pores. Thin sections were partially stained with Alizarin Red S and K-ferricyanide for carbonate mineral differentiation.

Twenty representative thin sections and core samples were observed using scanning electron microscopy (SEM), and the different types of elements in the samples were analyzed using an energy spectrum instrument (EDS). The morphological features of authigenic quartz and heavy minerals in the study area were analyzed using a Zeiss Crossbeam 550 FIB-SEM dual-beam electron microscope at the Reservoir Geology and Basin Analysis Key Laboratory of China University of Petroleum (RGBAKLCUP).

3.2. Geochemical analysis

For the fluid inclusion petrographic analysis and microthermometric measurements, 20 double-polished wafers approximately 0.05 mm in thickness were prepared. The fluid inclusion analysis was conducted using a microscope equipped with a 50 × objective combined with 10 × oculars and a calibrated Linkam THMSG600 heating–cooling stage, which can measure temperatures ranging from -196 °C to $+600$ °C. A homogenization temperature test was conducted on the fluid inclusions by applying an average heating rate of 10 °C/min when the temperature was lower than 60 °C and 3 °C/min when the temperature exceeded 60 °C. The precision of the temperature measurements for the homogenization temperature was ± 1 °C.

The contents of major and trace elements in the authigenic quartz of 10 representative thin sections of approximately 0.1 mm were analyzed via LA-ICP-MA at the State Key Laboratory of Ore Deposit Geochemistry, Institute of Geochemistry, Chinese Academy of Sciences, Guiyang, Guizhou Province, China. Laser sampling was performed using a GeoLas 2005 system with a cylindrical volume of approximately 40 cm^3. The operating conditions for the laser included a repetition rate of 8 Hz and an energy density of 10 J cm^{-2}. Each analysis spot size was 44 μm with a background acquisition of approximately 20 s (gas blank), followed by a data acquisition of 50 s.

Ten samples with a high calcite cement content at different well locations were selected for microdrilling sampling. The whole-rock powder of these sandstone samples and the drilled calcite powder (all through 200 mesh) were subjected to carbon-oxygen strontium isotope testing. Carbon and oxygen isotope testing was performed using a MAT-251EM gas stable isotope ratio mass spectrometer with resolution accuracies of $\delta^{13}C < 0.01‰$ and $\delta^{18}O < 0.02‰$. A fossil arrow stone carbonate (PDB) standard from the Lower Cretaceous Pee Dee Formation, South Carolina, USA, was used for carbon isotope analysis, and a standard mean seawater (SMOW) standard was used for oxygen isotope analysis using the equation $\delta^{18}O_{VSMOW} = 1.03086 \times \delta^{18}O_{VPDB} + 30.86$ (Frimmel, 2009). The Sr isotope test was completed using a NuInstrumen multi-receiver inductively coupled plasma mass spectrometer (MC-ICP-MS). The test data were corrected with $^{86}Sr/^{88}Sr = 0.1194$, and the data quality was monitored using international standard SRM-987. The mean value of the Sr isotope of the standard measured in this experiment was 0.710249 ± 0.000 003 (N = 7), with an analytical precision of >0.004%.

4. Results

4.1. Lithology

The reservoir rocks were dominated by fine-to coarse-grained sandstones, siltstones, and gravelly sandstones. The fine-to coarse-

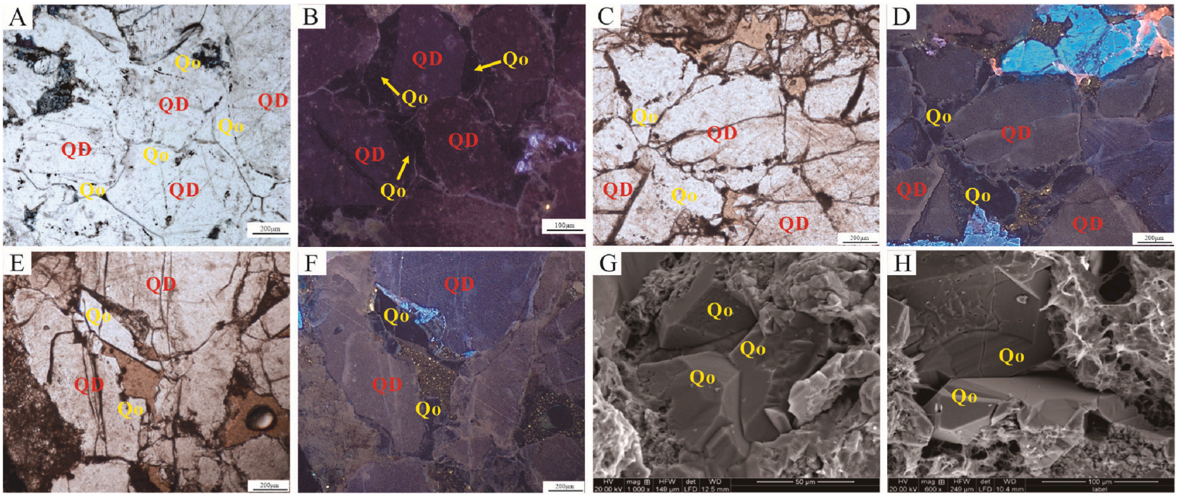

Fig. 4. Photomicrographs of authigenic quartz in the Lower Jurassic Ahe Formation sandstones, well YS4 and YN4. (A) YN4, 4467.3 m, Qo under plane-polarised light. The authigenic quartz is common, and the dust line is clear. (B) YN4, 4467.3 m, Qo is non-luminescent under CL. (C) YN4, 4496.65 m, Qo under plane-polarised light. (D) Same field view as that shown in panel (C). Qo is non-luminescent under CL. (E) YS4, 4042.1 m, Qo under plane-polarised light. (F) Same field view as that shown in panel (E). Qo is non-luminescent under CL. (G and H) YS4, 4007.8 m, SEM image showing Qo.
Qo—quartz overgrowth; QD—detrital quartz.

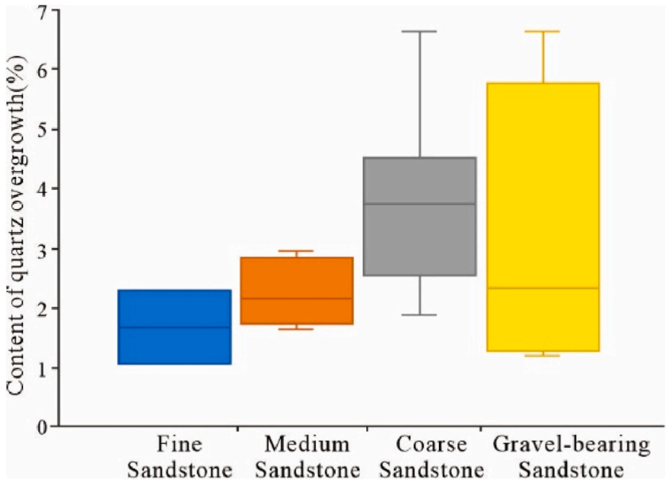

Fig. 5. Box plot of four types of sandstone against the content of Qo, well YS4. It shows variation in Qo with different types of sandstone. Qo—quartz overgrowth.

grained sandstones were moderately to well-sorted and the gravelly sandstones were poorly sorted. The detrital grains were sub-angular to sub-rounded, and the grain contacts were mainly short-to-long line contacts as well as point contacts (Fig. 3A). According to point counting, the sandstones were dominated by compositionally immature and feldspathic litharenite, with an average framework composition of $Q_{50}F_7R_{43}$ (Fig. 3B). The X-ray diffraction (XRD) analysis of the Lower Jurassic Ahe Formation sandstones in well YS4 revealed that the quartz content varied between 54% and 84%, with a mean value of 77.3%. K-feldspar and plagioclase (mainly albite) were the two major types of feldspar in the study area. The average K-feldspar content was 7.2%, varying from 4 to 10%. The plagioclase content ranged from 3 to 6%, with an average of 4.8%. The calcite content varied from 0 to 26%, with an average of 8.8%. The clay mineral content was 7–18%, with an average of 11.3%. The illite and kaolinite contents varied according to the clay fraction XRD data. Small amounts of mixed layers of illite, smectite (I/S), and chlorite were present. The composition of I/S showed a mainly interstratified order with R = 0.2 (I% = 20%).

4.2. *Authigenic quartz*

4.2.1. *Mineral characteristics*

Authigenic quartz was the most abundant cement in the Lower Jurassic Ahe Formation sandstones near the deep root fault (Fig. 4A and

Table 1
The content of quartz overgrowth, calcite cement and feldspar dissolution in Lower Jurassic Ahe Formation sandstone, well YS4.

Depth (m)	Quartz overgrowth (%)	Calcite (%)	Feldspar dissolution (%)	Depth (m)	Quartz overgrowth (%)	Calcite (%)	Feldspar dissolution (%)
3981.5	5.37		1.92	3998.55	3.45	0.18	2.16
3982	5.40		2.26	3999.05	2.90	1.25	3.74
3982.5	6.62		2.50	3999.7	1.93	0.94	1.77
3983	2.73		2.46	4000.25	4.46	0.13	1.34
3983.5	2.42		1.28	4000.5	2.55	1.14	3.41
3984	2.64		1.81	4006	3.21	2.41	1.48
3984.9	1.81		1.43	4006.7	2.93	0.58	1.32
3985.8	2.90		0.87	4007.8	3.31	2.97	0.75
3988.6	1.84		3.40	4041.5	2.14		4.66
3989.5	2.65		3.46	4041.85	1.90		2.79
3989.7	1.74		6.13	4042.1	1.54		0.41
3990.1	4.99		4.45	4043.55	4.77		0.63
3996.4	1.89	8.92	1.37	4046	3.63		0.48
3997.7	4.43	0.23	1.07	4046.5	3.73		0.82
3997.9	1.07		0.54				

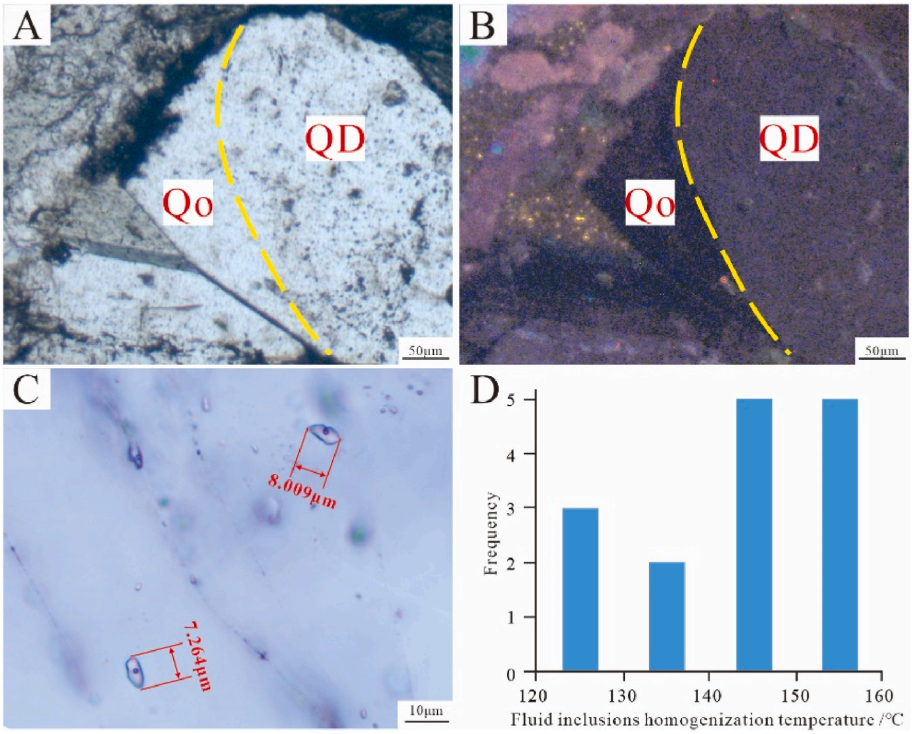

Fig. 6. Photomicrographs of aqueous inclusions within authigenic quartz, well YS4, 4042.1 m. (A) Qo under plane-polarised light. (B) Same field view as that shown in panel (A) under CL. (C) Aqueous inclusion in Qo in panel (A) under plane-polarised light. (D)Histogram of the homogenization temperature (Th) for the aqueous inclusions of authigenic quartz in the Lower Jurassic Ahe Formation sandstones near the deep-roots fault.
Qo—quartz overgrowth; QD—detrital quartz.

B). The most common form of authigenic quartz was quartz overgrowth (Qo) rimming the detrital grains in the Lower Jurassic Ahe Formation sandstones near the deep-rooted fault. Its area-delineated content in the thin sections ranged from 1.07 to 8.73%, with an average of 3.14%. Authigenic quartz generally exhibited non-luminescence (Fig. 4B, D, and F), which is most easily distinguished by its contrast with the dark brown or dark purple luminescence of detrital quartz. Qo mainly grew as multipoint and semi-ring grains based on the edge of detrital grains in the primary pore, and the dust traces were clear. The shape of the outer edge of Qo was relatively regular (Fig. 4D and F), and this feature was also evident under SEM (Fig. 4G and H). The Qo thickness commonly ranged from 30 to 120 μm and locally exceeded 150 μm. The authigenic quartz mainly developed one phase near the deep-rooted fault.

From a lithofacies point of view, Qo was the most developed in coarse sandstone in the Lower Jurassic Ahe Formation sandstones in well YS4 (Fig. 5). The Qo content in the coarse sandstone ranged from 1.89 to 6.62%, with an average of 3.71% (Table 1), which was much higher than that of the other lithofacies.

4.2.2. *Geochemical characteristics*

4.2.2.1. Fluid inclusions. Aqueous inclusions were present in the authigenic quartz in the Lower Jurassic Ahe Formation sandstones near the deep root fault, which mainly existed in the quartz overgrowth. The measured sizes of the aqueous inclusions ranged from 3 to 8 μm (Fig. 6C). Aqueous inclusions were measured in the quartz overgrowths of the Lower Jurassic Ahe Formation sandstones. Fig. 7 indicates the variation of the size of the gas phase during the heating and cooling processes. After the heating and cooling processes of inclusions in quartz overgrowth, there was no change in the size of the gas phase when the inclusions were returned to room temperature after Th measurement (Fig. 7D, I). The phases of the measured inclusions and their corresponding homogenization temperatures (Th) and the freezing points are listed in Table 2. The Th of authigenic quartz in the Lower Jurassic Ahe Formation sandstones ranged from 120 to 160 °C and the freezing points ranged from −0.4–0.2 °C (Fig. 6D, Table 2).

4.2.2.2. Element geochemistry. The LA-ICP-MS analyses revealed that the contents of major and trace elements at majority of test points of quartz overgrowth in the sandstone reservoir were different from those of quartz particles. Among the tested major and trace elements, Li, Na, K, Ge, Rb, and Sr exhibited a particularly notable difference in terms of the order of magnitude (Fig. 8, Table 3).

4.3. *Calcite*

4.3.1. *Mineral characteristics*

Calcite is the dominant carbonate cement and is well-developed in the Lower Jurassic Ahe Formation sandstone. Its area-delineated content in the thin sections ranges from 0 to 8.92%, with an average of 1.47% (Table 1). The thin section and SEM investigations revealed that calcite was mainly cemented using two types of cementation methods. The main type was grain-to-grain cementation, which occurred in the primary pores after quartz overgrowth cementation (Fig. 9A, B, and C). The other was intragranular cementation, which was filled with feldspar secondary dissolution pores (feldspar dissolution pores formed during the early diagenetic stage) (Fig. 9B). The formation period of calcite cementation is visibly later than that of quartz overgrowth. The calcite cementation exhibited mainly dark orange luminescence (Fig. 9B).

4.3.2. *Geochemical characteristics*

The calcite cements in Lower Jurassic Ahe Formation, as revealed by Electron Microprobe Analysis (EMPA), had similar Ca compositions (Table 4; Fig. 10A). Calcium was used as the correction standard with a unified percentage of 65% (Table 4). The Fe concentrations in the calcite cements were 0.39–0.88%, with an average value of 0.62% (Table 4). The average concentration of Mn was 0.48%, ranging from 0.29 to 0.82% (Table 4). The Mg concentration ranged from 0.25 to 1.14%, with an average value of 0.62% (Table 4). In addition, Si and Al impurities were high in the calcite cement samples (Table 4). The Co and Ni contents in the calcite cements were generally high (Table 4; Fig. 10B).

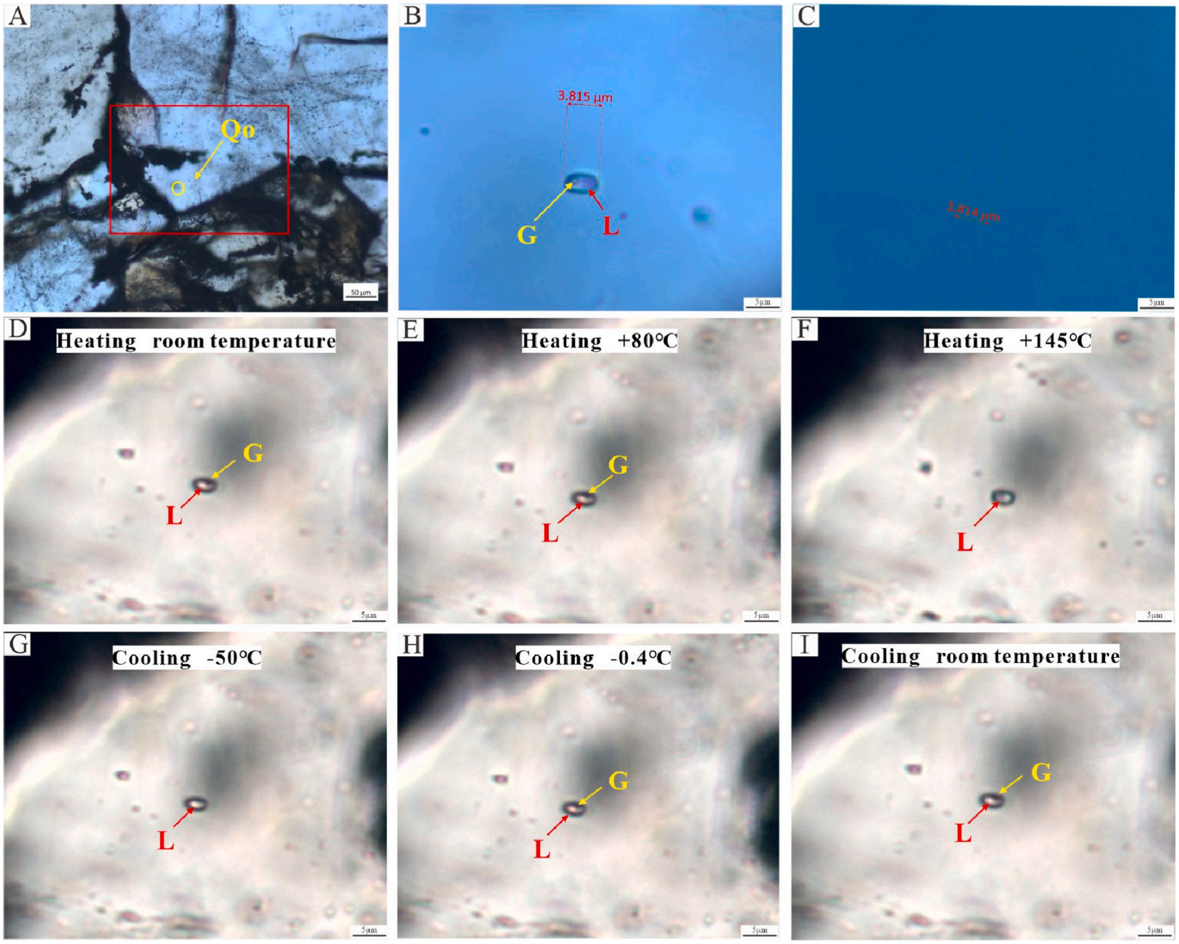

Fig. 7. Images of aqueous fluid inclusions (AFI) in quartz overgrowth at 4496.64 m in well YN4. (A) Inclusion contained in quartz overgrowth. (B) Aqueous inclusions in Qo under plane-polarised light at room temperature. (C) Same field view as that shown in panel (B) under ultraviolet light, with the aqueous inclusion showing non-fluorescence. (D–I) The variation of the size of gas phase in inclusion during heating and cooling processes.
Qo-quartz overgrowth; G-gas phase; L-liquid phase.

Table 2
Micro-thermometric data of the aqueous inclusions in the Lower Jurassic Ahe Formation sandstones near the deep-roots fault. Th: homogenization temperature.

Well	Depth (m)	Th (°C)	Tm (°C)	Well	Depth (m)	Th (°C)	Tm (°C)
YS4	4000.78	152	−0.2	YN4	4496.64	152	−0.4
YS4	4000.78	143	−0.2	YN4	4496.64	153	−0.3
YS4	4000.78	128	−0.2	YN4	4496.64	144	−0.4
YS4	4000.78	133	−0.1	YN4	4496.64	144	−0.4
YN4	4474.20	156	−0.4	YN4	4496.64	125	−0.2
YN4	4496.64	150	−0.4	YN4	4603.57	126	−0.4
YN4	4496.64	145	−0.4	YN4	4603.57	153	−0.4
YN4	4496.64	147	−0.3	YN4	4603.57	133	−0.3
YN4	4496.64	149	−0.3				

5. Discussion

Significant deformation and uplift of the South Tian Shan began at approximately 36 Ma, becoming more evident from approximately 13 Ma, culminating from 6.5 Ma, and reaching its peak after 2.6 Ma (T. Zhang et al., 2014). The Kuqa thrust-fold system showed that the tectonic deformation of the Kuqa depression strengthened gradually and propagated southward into the basin. The northern monocline belt was formed during the deposition of the Jidike Formation (36–13 Ma) and the Kelasue-Yiqikelike structural belt formed mainly during the deposition of the Kangcun Formation (13–6.5 Ma). Previous studies have also suggested stepwise deformation in the Kuqa depression since the Cenozoic era (Chen et al., 2004; Jia et al., 2003; Jia and Li, 2008; Liu et al., 2000; Lu et al., 1997; Yin et al., 1998; Zeng, 2004). Therefore, we speculated that the formation time of the deep-rooted fault (Yiqikelike fault) during the Jidike Formation was earlier than the rapid shortening of the Kuqa depression.

In the context of such strong and complex tectonic activities, diagenetic fluids are characterized by multiple phases, types, and complex sources. It is important to understand the types of diagenetic fluids that influence diagenesis to investigate the reasons for the differences in diagenetic characteristics, especially between those close to the deep-rooted fault and those far from it.

By observing the thin sections and determining the cement content in thin sections in well YS4, Qo content in the coarse sandstone decreases with the increase in lateral distance from the deep-rooted fault (Fig. 11A). This phenomenon is also notable in calcite, in which the calcite content is relatively high closer to the deep-rooted fault (Fig. 11B). As a result, the deep fluid was likely to migrate into the Lower Jurassic Ahe Formation sandstone reservoirs through the deep-rooted fault and participate in diagenesis.

5.1. *Evidence of deep fluid activity from authigenic quartz*

During burial diagenesis, the sources of siliceous material in sandstone reservoirs are mainly the dissolution of feldspar, siliceous released

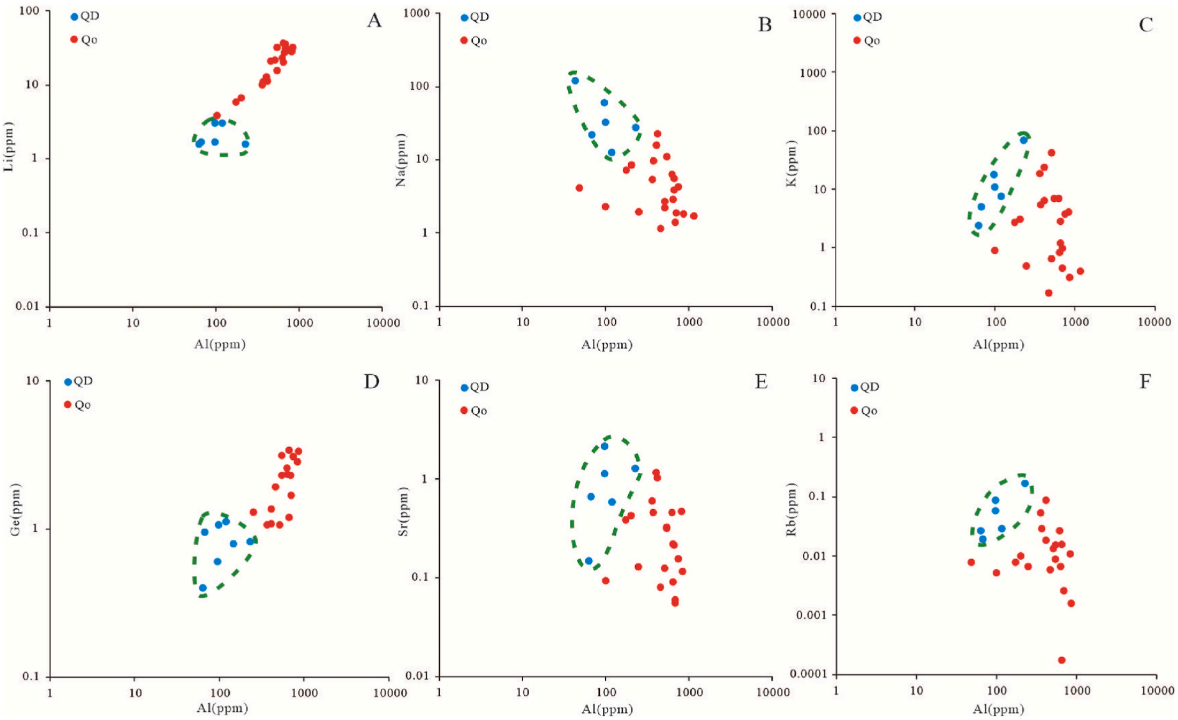

Fig. 8. Correlation of trace elements: (A) Li versus Al; (B) Na versus Al; (C) K versus Al; (D) Ge versus Al; (E) Sr versus Al; (F) Rb versus Al. The element concentration was measured by LA-ICP-MS. The green dashed line represents the range of elements in the detrital quartz grains.
Qo—quartz overgrowth; QD—detrital quartz.

Table 3
Results of the LA-ICP-MS analysis for authigenic quartz in the Lower Jurassic Ahe Formation sandstone reservoirs.

Well	Sample	Position	Li	Na	Al	K	Ge	Rb	Sr
YS4	1	QD	1.68	60.88	96.84	17.86	0.61	0.09	2.12
YS4	2	QD	2.99	12.74	118.92	7.59	1.12	0.03	0.59
YS4	3	Qo	31.66	11.03	549.57	6.88	2.30	0.02	0.32
YS4	4	Qo	31.88	1.84	860.25	0.31	3.36	0.00	0.12
YS4	5	Qo	23.19	6.22	630.74	7.04	2.60	0.03	0.45
YS4	6	Qo	35.32	1.38	690.97	0.45	2.31	0.00	0.06
YS4	7	Qo	29.43	4.26	748.61	3.76	3.11	0.00	0.16
YS4	8	Qo	21.25	1.14	466.51	0.17	1.94	0.01	0.08
YS4	9	Qo	36.99	2.91	643.35	0.83	2.33	0.01	0.09
YS4	10	Qo	21.65	2.68	515.14	0.65	1.08	0.01	0.12
YS4	11	Qo	15.70	0.00	552.72	0.00	3.13	0.01	0.32
YS4	12	Qo	11.33	22.28	416.40	6.48	1.36	0.02	1.02
YS4	13	Qo	10.85	9.74	371.22	5.51	1.07	0.03	0.46
YN4	14	QD	1.57	27.99	229.47	68.04	0.82	0.17	1.29
YN4	15	QD	1.66	22.23	68.15	5.01	0.95	0.02	0.65
YN4	16	QD	3.03	32.80	98.51	11.11	1.07	0.06	1.14
YN4	17	QD	0.08	0.93	7.72	0.14	1.23	0.00	0.01
YN4	18	QD	1.60	0.00	63.14	2.41	0.40	0.03	0.15
YN4	19	Qo	6.60	8.43	203.33	3.03	1.01	0.01	0.42
YN4	20	Qo	4.14	2.28	100.35	0.89	0.17	0.01	0.09
YN4	21	Qo	5.83	7.13	175.22	2.72	0.93	0.01	0.39
YN4	22	Qo	28.14	0.00	832.10	4.10	2.86	0.01	0.47
YN4	23	Qo	13.01	15.97	415.35	23.37	1.09	0.09	1.15
YN4	24	Qo	10.18	5.29	363.45	18.82	1.07	0.05	0.60
YN4	25	Qo	20.32	5.49	662.14	2.89	3.41	0.02	0.22
YN4	26	Qo	31.29	1.88	701.41	0.99	1.68	0.00	0.05
YN4	27	Qo	27.45	3.86	663.50	1.20	1.19	0.00	0.21

from the pressure dissolution of siliceous clastic particles, and the transformation of clay minerals and siliceous material from outside the sand body (McBride, 1989; Renard et al., 2000; Worden and Morad, 2000; Worden and Morad, 2009; Bjørlykke and Jahren, 2012; Yuan Tao et al., 2017).

The first thing to discuss is what the source of silica is. In the thin sections, the quartz overgrowth was already cemented before strong compaction in the Lower Jurassic Ahe Formation sandstones near the deep-rooted fault (Fig. 4A–F). Furthermore, in terms of chemical composition, the contents of major and trace elements of quartz overgrowth were different from those of quartz particles in the sandstone reservoirs near the deep-rooted fault (Fig. 8). Therefore, the main source of siliceous material was provided by other sources instead of pressure solution.

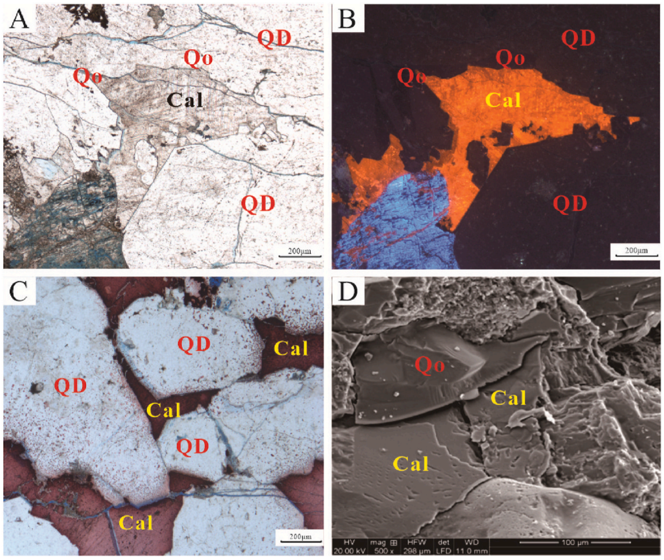

Fig. 9. Photomicrographs of calcite in the Lower Jurassic Ahe Formation sandstones, well YS4 and YN4. (A) YN4, 4496.65 m, Cal under plane-polarised light. (B) Same field view as that shown in panel (A). Cal is dark orange luminescent under CL. (C) YS4, 4007.8 m, Cal under plane-polarised light. Cal is dyed red by a mixture of alizarin red and potassium ferricyanide. (D) YS4, 4007.8 m, SEM image showing Qo and Cal.
Qo—quartz overgrowth; QD—detrital quartz; Cal—Calcite.

Authigenic kaolinite developed in the J_1a sandstone near the deep-rooted fault in the inter-granular pores (Fig. 12A). Vermicular and pseudohexagonal flaky kaolinite was extensively developed in the primary and secondary pores (Fig. 12B). During the dissolution of feldspar minerals, a large number of dissolution products are produced, primarily illite and kaolinite. The occurrence of authigenic kaolinite suggests that feldspar dissolution is a possible source. According to the dissolution of potassium feldspar, authigenic clay mineral kaolinite was first formed in the early dissolution, and the main reaction equation is as follows (Rezaee and Tingate, 1997):

$$2KAlSi_3O_8 + 2H_2CO_3 + H_2O \rightarrow Al_2Si_2O_5(OH)_4 + 4SiO_2 + 2K^+ + 2HCO_3^-$$

Assuming that all kaolinite was formed by the dissolution of potassium feldspar (Wang and Long, 2010), the siliceous content ranged from 0.06 to 5.53%, with an average of 2.16%, while the content of quartz enlarged edges ranged from 0.41 to 8.73%, with an average of 3.71%. The siliceous content provided by dissolution was insufficient to achieve the actual quartz oversize content. Additionally, the correlation between the dissolution amount of feldspar and the authigenic quartz content was poor (Fig. 12). The conversion of kaolinite to illite initiated at approximately 70 °C; however, this phenomenon occurs most commonly from 130 °C (Worden and Burley, 2003). As the strata in the study area were rapidly buried from the late Cretaceous period, a large amount of kaolinite can be regarded as the product of late diagenesis. Owing to the relatively high content of silica cement, the siliceous material released from the dissolution of feldspar was not the main source of phase I quartz overgrowth in the Lower Jurassic Ahe Formation sandstones near the deep-rooted fault.

Excluding endogenous sources, deep fluid as a source of siliceous is the correct extrapolate direction, combined with the background of strong tectonic activity events and the positive correlation between

Table 4
Major and trace elements results of the LA-ICP-MS analysis for carbonate cements in the Lower Jurassic Ahe Formation sandstone reservoirs. Calcium is as a correction standard.

Well	Sample	Na	Mg	Al	Si	K	Ca	Ti	Fe	Mn	Cr	Co	Ni
YS4	1	0.0194	0.6624	1.4307	1.8871	0.6207	65.5000	0.0011	0.5462	0.2877	0.0006	1.8405	5.3417
YS4	2	0.0471	0.7177	3.3869	4.4075	1.4883	65.5000	0.0019	0.7045	0.8219	0.0015	2.6575	6.2842
YS4	3	0.0425	0.8471	3.6392	4.7677	1.6693	65.5000	0.0024	0.7421	0.5309	0.0015	2.5800	6.7630
YS4	4	0.0770	1.1370	5.9870	7.7905	2.7382	65.5000	0.0725	0.8752	0.4435	0.0022	5.1907	8.5912
YS4	5	0.0215	0.7499	2.1277	2.6445	0.8927	65.5000	0.0020	0.7301	0.3775	0.0009	0.8476	0.8932
YS4	6	0.0232	0.7016	1.7135	2.1021	0.7198	65.5000	0.0027	0.7432	0.4021	0.0010	1.0432	2.2096
YS4	7	0.0164	0.3288	0.9147	1.1562	0.3230	65.5000	0.0061	0.4819	0.5526	0.0011	0.4481	0.9310
YS4	8	0.0295	0.3166	0.6056	0.7239	0.0382	65.5000	0.0035	0.4884	0.4053	0.0006	0.6371	1.9427
YS4	9	0.0092	0.3506	0.3801	0.4606	0.0031	65.5000	0.0002	0.4396	0.3295	0.0006	3.4046	8.0942
YS4	10	0.0081	0.2544	0.2950	0.3880	0.0181	65.5000	0.0011	0.3871	0.4711	0.0004	1.4337	8.4598

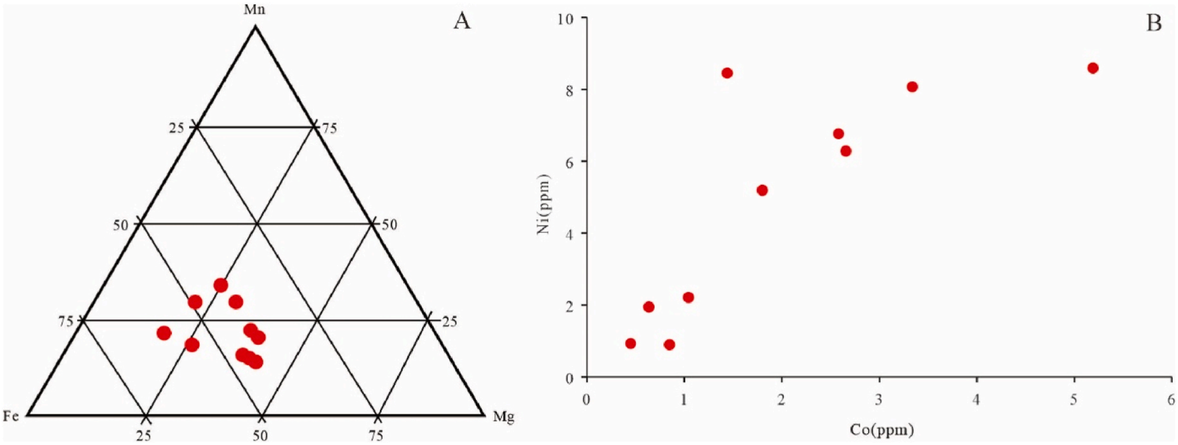

Fig. 10. Elemental Geochemical Characteristics of Calcite in the deep fracture: (A) Ternary diagrams showing elemental geochemistry (wt. %) characteristics, (B) Cross plot of Co and Ni.

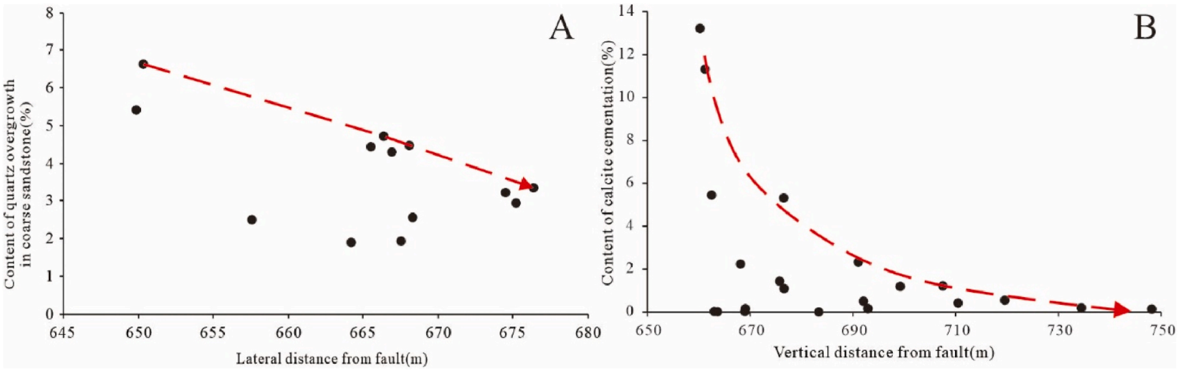

Fig. 11. (A) Cross plot of lateral distance from the deep-rooted fault against the content of Qo, well YS4. (B) Cross plot of vertical distance from the deep-rooted fault against the content of calcite cementation in well YS4. Both show negative correlation in content with distance. Qo—quartz overgrowth.

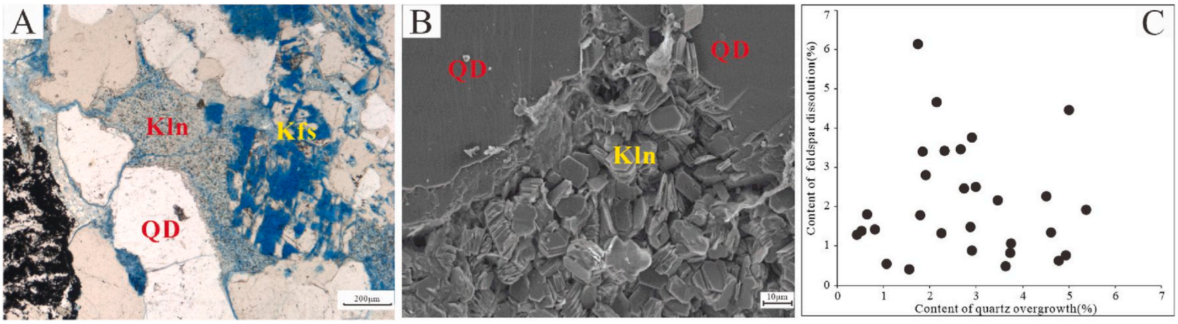

Fig. 12. (A) YS4, 3980.7 m, feldspar dissolution under plane-polarised light. (B) YS4, 4005.5 m, authigenic kaolinite developes in the intergranular pores under SEM. (C) Cross plot of the content of Qo against the content of feldspar dissolution in well YS4.
Kln—Kaolinite; QD—detrital quartz; Kfs—K-feldspa.

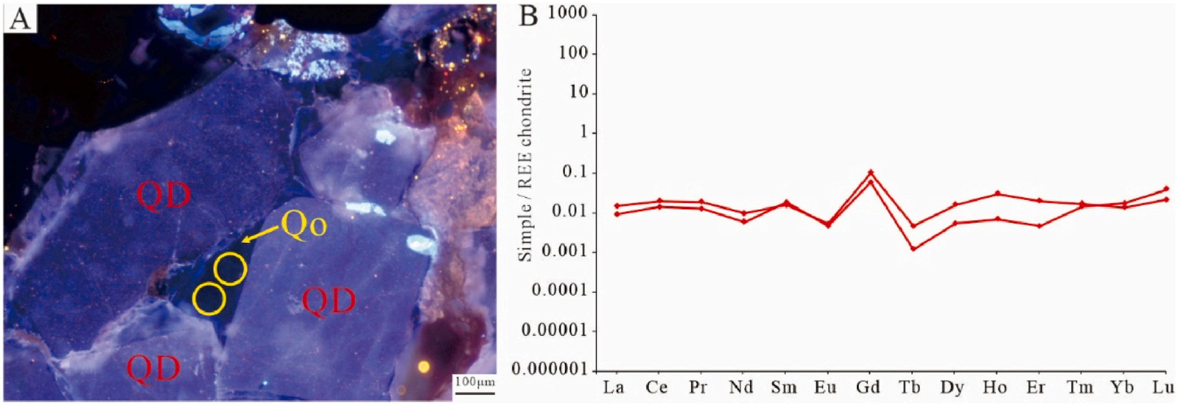

Fig. 13. (A) Points of authigenic quartz, well YS4, 4007.8 m. (B) Rare earth element (REE) patterns of quartz. Each line in the distribution map represents each point tested in different samples by LA-ICP-MS. The original data are given in Table 5.
Qo—quartz overgrowth; QD—detrital quartz.

cement content and fault distance (Fig. 11). Hydrothermal siliceous rocks are a special source of siliceous rocks in sandstone reservoirs (Rusk et al., 2008; Worden and Morad, 2009; Yuan et al., 2017). Hydrothermal fluids can travel long distances along faults and fractures, thereby providing material sources for sandstone reservoirs (Pirajno, 1992; Zhai et al., 2003; Larsen et al., 2009; Chen et al., 2011; Liu et al., 2017).

Fluid inclusions can provide valuable information regarding the temperature and timing of mineral diagenesis (Bjørlykke and Egeberg, 1993; Makowitz et al., 2006). The maximum temperature of Lower Jurassic Ahe Formation was 100 °C before the rapid burial stage (Ni et al., 2022), and the temperature of deep fluid is at least 5 °C higher than that of the surrounding environment (Pirajno, 1992; Rusk et al., 2008). The values of most aqueous inclusions in the quartz overgrowth in the Lower Jurassic Ahe Formation sandstones ranged from 120 to 160 °C (Fig. 6D) and were considerable higher than the maximum burial temperatures. Therefore, it is speculated that the Lower Jurassic Ahe Formation sandstones near the deep-rooted fault experienced deep fluid filling.

Eu showed a slight negative abnormality in the quartz overgrowth (Fig. 13B). Higher temperature will lead to the decrease of Eu^{3+}in the fluid (Wu et al., 2023), meanwhile, the decrease of Eu^{3+}in the fluid will result in a relatively low Eu content in the precipitated authigenic minerals (Zhao et al., 2018). Therefore, the precipitation of quartz overgrowth in the Lower Jurassic Ahe Formation sandstones was

Table 5
Rare earths elements results of the LA-ICP-MS analysis for quartz overgrowth and carbonate cements in the Lower Jurassic Ahe Formation sandstone reservoirs.

Sample	La (ppm)	Ce (ppm)	Pr (ppm)	Nd (ppm)	Sm (ppm)	Eu (ppm)	Gd (ppm)	Tb (ppm)	Dy (ppm)	Ho (ppm)	Er (ppm)	Tm (ppm)	Yb (ppm)	Lu (ppm)	δEu
Qo-1	0.0150	0.0201	0.0192	0.0091	0.0159	0.0055	0.1028	0.0048	0.0165	0.0305	0.0203	0.0175	0.0140	0.0217	
Qo-2	0.0094	0.0144	0.0129	0.0060	0.0186	0.0046	0.0596	0.0010	0.0055	0.0070	0.0047	0.0147	0.0179	0.0403	
Cal-1	0.8599	0.9837	0.8444	0.9080	1.1169	1.7583	1.3085	1.1549	1.4661	1.1638	1.0988	1.0502	1.2843	0.9761	1.45
Cal-2	0.7493	0.8485	0.7488	0.8358	1.0678	1.6634	1.2762	1.2890	1.6667	1.3660	1.1685	1.1070	1.3111	1.1183	1.42
Cal-3	1.9800	2.2765	1.8605	2.0996	2.5340	3.7927	3.0112	2.8761	3.2930	2.6463	2.7000	2.8075	2.8971	2.4327	1.37
Cal-4	1.8378	2.1509	1.7775	1.9305	2.4597	3.6301	2.9973	2.7671	3.2309	2.5299	2.6463	2.5371	2.9519	2.3767	1.34
Cal-5	1.2960	1.4787	1.2867	1.4322	1.8315	2.9040	2.3794	2.1798	2.6200	2.1488	2.1839	2.0506	2.4138	1.8167	1.39
Cal-6	1.0662	1.1899	1.0371	1.2056	1.4921	2.5239	2.0190	1.9234	2.3425	2.0089	2.0078	2.0639	2.1526	1.8325	1.45

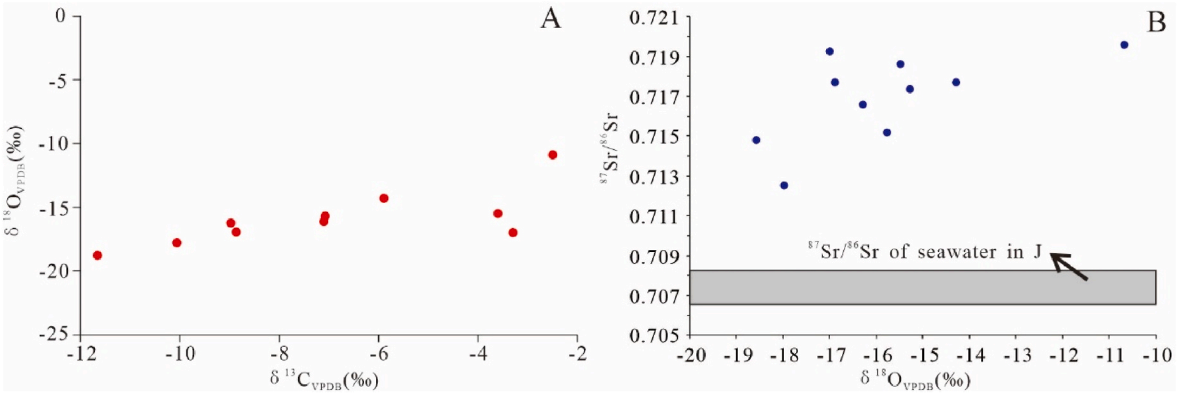

Fig. 14. (A) $\delta^{18}O$ versus $\delta^{13}C$ for calcite, (B) $^{87}Sr/^{86}Sr$ versus $\delta^{18}O$ for calcite. Samples were from Lower Jurassic Ahe Formation sandstones in the deep-rooted fault.

Table 6
Isotope values of calcite are given for Lower Jurassic Ahe Formation sandstone of the well YN4 and YS4.

Well	Depth (m)	$^{87}Sr/^{86}Sr$	$\delta^{13}C_{VPDB}$ (‰)	$\delta^{18}O_{VPDB}$ (‰)	Well	Depth (m)	$^{87}Sr/^{86}Sr$	$\delta^{13}C_{VPDB}$ (‰)	$\delta^{18}O_{VPDB}$ (‰)
YS4	3996.40	0.71498048	−11.7	−18.6	YS4	4007.80	0.71538587	−7.1	−15.8
YS4	4000.50	0.71676685	−9.0	−16.3	YS4	4043.00	0.71976105	−2.5	−10.7
YS4	4005.00	0.71945425	−3.3	−17.0	YN4	4453.95	0.71271797	−10.1	−18.0
YS4	4005.50	0.71881761	−3.6	−15.5	YN4	4464.66	0.71788981	−5.9	−14.3
YS4	4006.00	0.71753982	−7.0	−15.3	YN4	4476.75	0.71788390	−8.8	−16.9

obviously affected by deep fluid.

Combined with previous studies, the characteristics of abnormally high temperatures of siliceous cement fluid inclusions, hydrothermal mineral assemblage, main and trace elements and rare earth elements in siliceous cement, and fault activity indicate that hydrothermal fluid is an important source of siliceous cement in the Lower Jurassic Ahe Formation sandstone near the deep-rooted fault..

5.2. *Evidence of deep fluid activity from calcite cements*

Zhu et al. (2012) simulated the interaction between a deep CO_2-rich fluid and the surrounding rock in the Taichung area using the thermodynamic model of Duan and Li (2008). The calculation results revealed that the solubility of $CaCO_3$ in CO_2-rich deep fluid increased to a maximum at a certain depth during the transport from deep to shallow, and then the solubility started to decrease gradually to shallow. The deep fluid can result in the deep dissolution of carbonate rock and shallow precipitation of carbonate minerals. Several researchers have studied the significant dissolution of deep fluids in Lower Paleozoic carbonates in the Tarim Basin (Lv et al., 2005; Jin et al., 2006; Lv et al., 2008; Zhu et al., 2008). Significant dissolution occurred in relatively deep Lower Ordovician carbonates, and significant calcite infilling occurred in relatively shallow Ordovician carbonates and Silurian sandstones in the Taichung area (Zhu et al., 2012). Therefore, given the aforementioned example, the strong calcite cementation in the Jurassic Ahe Formation, which is located in shallower strata, can be reasonably inferred to be caused by the upward movement of deep CO_2-rich fluids along the deep-rooted fault.

The carbonate cements were characterized by low negative $\delta^{13}C_{(V\text{-}PDB)}$ values in the Lower Jurassic Ahe Formation sandstone reservoirs, ranging from −11.70‰ to −2.50‰ (Fig. 14A; Table 6). The normal value of the $\delta^{13}C$ of CO_2 in the mantle environment varies from −10‰ to 0‰ (Deines, 1992) and the lighter composition of $\delta^{13}C$ represents that the original carbon of the mantle may reflect recirculating crustal source material caused by plate subduction (Deines, 1992) or multi-stage degassing of the mantle (Milledge H J et al., 1983; Trull T et al., 1993). By combining the results of previous studies with tectonic activities, it can be inferred that the diagenesis was influenced by deep fluids near the deep-rooted fault.

Generally, the $^{87}Sr/^{86}Sr$ ratio was not fractionated by physical, chemical, or biological processes but was mainly controlled by the source of strontium. In this study, we used data from hundreds of samples collected in many countries and described by researchers (Podlaha, 1995; Podlaha et al., 1998; Podlaha et al. Ján Veizer et al., 1999) and tested the Jurassic era with a value ranging from 0.7066 to 0.7083 as the background value of the Lower Jurassic sandstone. As shown in Fig. 14B, the Sr isotope value is higher than that of seawater in the same period, which was likely affected by other fluids (Hu et al., 2018). Atmospheric precipitation interacting with surface clastic materials or deep hydrothermal fluids interacting with deep clastic strata can result in fluids

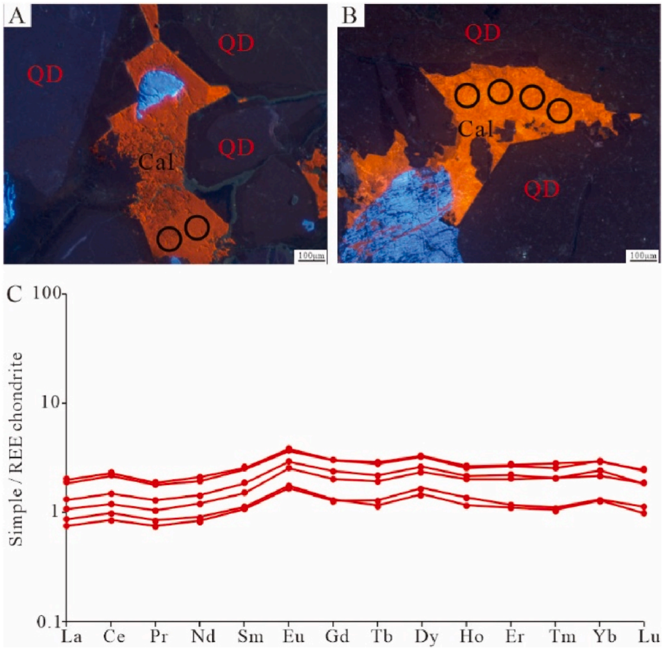

Fig. 15. (A–B) Points of calcite, well YS4, 4005 m. (C) Rare earth element (REE) patterns of calcite. Each line in the distribution map represents each point tested in different samples by LA-ICP-MS. The original data are given in Table 5.
Cal—calcite; QD—detrital quartz.

with high $^{87}Sr/^{86}Sr$ values. Given the $\delta^{13}C$ results for these samples, the higher $^{87}Sr/^{86}Sr$ values of the samples are considered to be related to deep fluids, which is consistent with the results of Cai et al. (2008) and Zhu et al. (2012).

Eu showed a slight positive abnormality in calcite (Fig. 15C). δEu typically has an average value of 0.233 in carbonates (Turekian and Wedepohl, 1961) and average value of 0.411 in the crust (Taylor, 1964). δEu $[Eu/(Sm \times Gd)^{1/2}] > 1$ is a geochemical indicator commonly used in hydrothermal fluid analyses (Young, 1999; Lawrence et al., 2006). Owing to the presence of a deep mantle source material, δEu increases and approaches 1 or >1. δEu ranges from 1.34 to 1.45, showing the overall influence of deep fluids.

Several trace elements, including Fe, Mn, Al, Ni, Cu, Zn, and Co, have also been used to indicate hydrothermal genetic minerals (Savelli et al., 1999). These trace elements are enriched in calcite in the Lower Jurassic Ahe Formation sandstones. Therefore, the precipitation of calcite in the Lower Jurassic Ahe Formation sandstone was affected by the hydrothermal fluid. Moreover, the contents of Co and Ni in the calcite cements were generally high, indicating that the formation of ferruginous calcite may be associated with deep fluids (Allegre and Michard, 1973, Table 4, Fig. 10B).

According to Cai et al. (2008), one of the origins of hydrothermal rutile is the formation of high titanium rocks through hydrothermal alteration. The lithology of the study area is mainly detrital sandstone and feldspar detrital sandstone, among which the detritus mainly includes schist debris, chlorite, amphibole, and biotite, and the content of biotite particles is not low. The deep fluid after the formation of the first-order fault underwent hydrothermal alteration with schist-rich cuttings and biotite particles during the migration process to precipitate Ti from chlorite and biotite. When the Ti-rich fluid enters the primary dissolved pores or feldspar dissolves the secondary pores, short columnar rutile is formed (Fig. 16A and B). In addition, the pleochroism of rutile is a weak reddish-brown-strong blood-red internal reflection under polarised light (Cai et al., 2008). The rutile in this study area also exhibits this feature under polarised light (Fig. 16F). Moreover, rutile is frequently associated with calcite (Fig. 16D and E), and sometimes occurs in association with quartz overgrowth (Fig. 16C), which may also indicate that the formation of rutile is related to deep fluids.

5.3. *The impacts on reservoir quality of deep fluid*

Unlike the "very developed Phase I quartz overgrowth and Phase I calcite" cementation characteristics of the area near the deep-rooted fault, the authigenic quartz and calcite of the area far from the deep-rooted fault had the following cementation characteristics.

Authigenic quartz mainly occurred as quartz overgrowth (Qo) and micro quartz (Qm). Qo was not well developed and exhibited brown luminescence (Fig. 17A–D). Qm was more developed with a regular shape around the periphery of the Qo and in the secondary pores produced by feldspar dissolution and brown luminescence or non-luminescence (Fig. 17A, B, E, F). Calcite was developed in two phases. Early calcite cementation mainly developed in the intergranular pores and bright yellow luminescence (Fig. 17H). Late calcite cementation mostly developed in secondary dissolved pores and dark orange

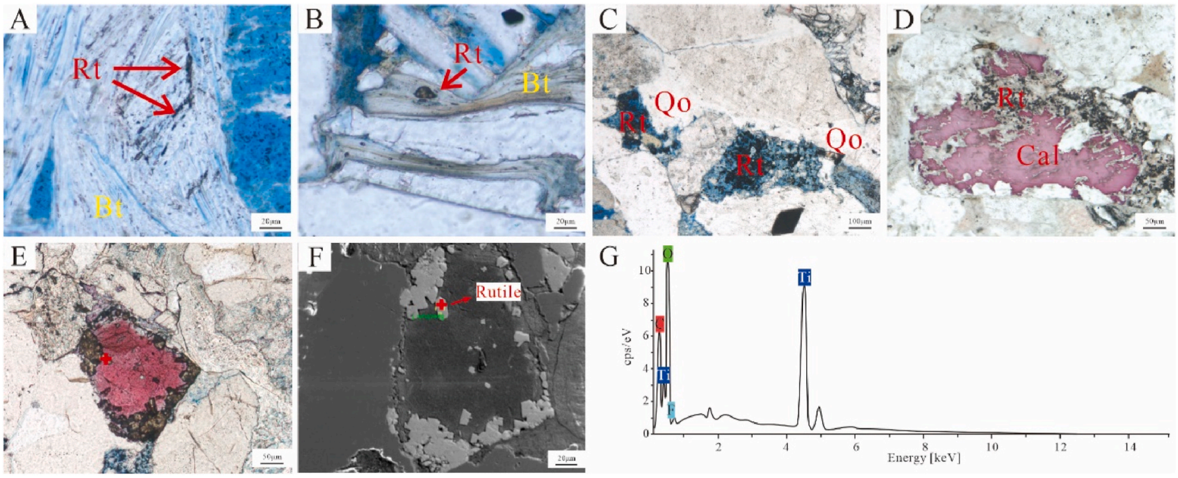

Fig. 16. Photomicrographs of authigenic heavy minerals in the Lower Jurassic Ahe Formation sandstones, well YS4. (A–B) 4000.5 m. Rt under plane-polarised light. Altered biotite precipitates dark authigenic mineral rutile. (C) 4041.5 m. The commensalism of Rt and Qa under plane-polarised light. (D) 3987.8 m. The commensalism of Rt and Cal under plane-polarised light. (E) 3987.8 m, Rt under plane-polarised light. (F) Same field view as that shown in panel (E). Rt under SEM. (G) The EDS of mark site in M showing the rutile.
Qo—quartz overgrowth; Cal—Calcite; Rt—Rutile; Bt—Biotite.

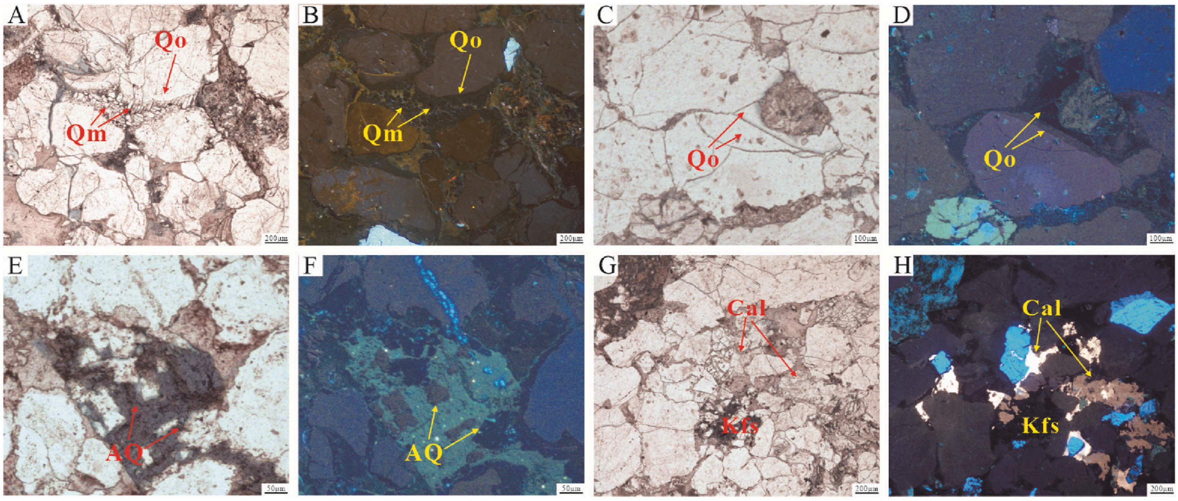

Fig. 17. The different colors of quartz overgrowth and calcite of four structural sites. (A) DB102, 4981.5 m, Qo and Qm under plane-polarised light. (B) Same field view as that shown in panel (A). Qo and Qm shows brown under CL. (C) TZ2, 4403.32 m, multi-period of Qo under plane-polarised light. (D) Same field view as that shown in panel (C). Multi-period of Qo show non-luminescent and brown under CL. (E) DB102, 4937.5 m, authigenic quartz filling secondary feldspar dissolution pores under plane-polarised light. (F) Same field view as that shown in panel (E). Authigenic quartz filling secondary feldspar dissolution pores show non-luminescent and brown under CL. (G) TZ2, 4345.3 m, multi-period of Cal under plane-polarised light. (H) Same field view as that shown in panel (I). Multi-period of Cal show light yellow and dark orange under CL.
Qo—quartz overgrowth; Qm—micro quartz; AQ—authigenic quartz; Cal—Calcite.

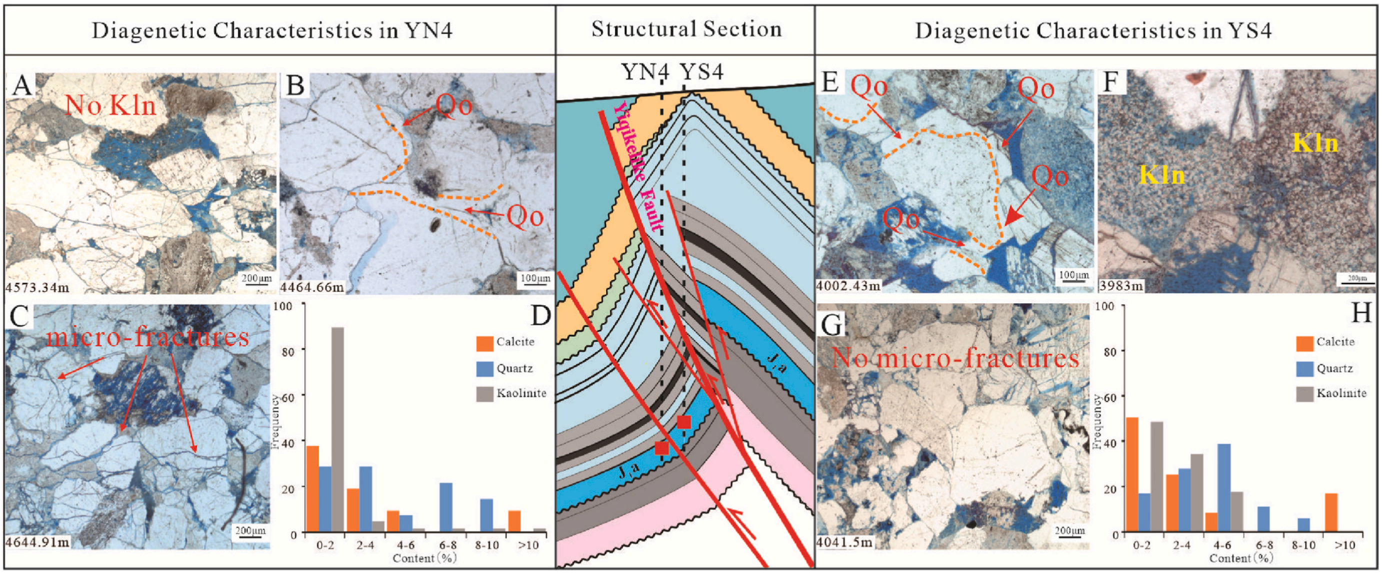

Fig. 18. Diagenetic differences between well YS4 and well YN4 in Lower Jurassic Ahe Formation sandstone. (A) YN4, 4573.34 m, few kaolinite under plane-polarised light. (B) YN4, 4464.66 m, Qo under plane-polarised light. (C) YN4, 4644.91 m, many micro-fractures under plane-polarised light. (D) Frequency histogram of calcite, quartz overgrowth and kaolinite in well YN4. (E) YS4, 4002.43 m, Qo under plane-polarised light. (F) YS4, 3983 m, a lot of kaolinite under plane-polarised light. (G) YS4, 4041.5 m, few micro-fractures under plane-polarised light. (H)Frequency histogram of calcite, quartz overgrowth and kaolinite in well YS4.
Qo—quartz overgrowth; Kln—Kaolinite.

luminescence (Fig. 17H). The cementation characteristics in terms of the phase, type, and cathodoluminescence color of authigenic quartz and calcite far from the deep-rooted fault differed significantly from those near the deep-rooted fault.

Regarding the structural profile, the Ahe Formation in well YS4 was closer to the deep-rooted fault than the Ahe Formation in well YN4 (Fig. 18). The Ahe Formation in well YS4 is located in the footwall of the deep-rooted fault, and the Ahe Formation in well YN4 is located in the footwall of the deep-rooted fault, as well as the footwall of the second-order fault. The compaction in well YN4 was significantly stronger than that in well YS4, and the micro-fractures were more developed (Fig. 18C and G) because well YN4 is closer to the second-order fault. Micro-fractures, mainly due to overlying ground pressure and the lateral extrusion of tectonic stress, cause rigid fragile particles to break along the vulnerable surface (Li et al., 2007; Nan et al., 2007). Based on the area-delineated content of Qo in the thin sections, that in well YS4 was higher than that in well YN4 (Fig. 18D and H). The shape of the outer edges of the Qo in well YN4 was not very regular, with the edges touching each other, also suggesting stronger compaction in well YN4 (Fig. 18B and E). The development of micro-fractures in well YN4 also led to a difference in the kaolinite content (Fig. 18D and H, Table 7) and supported kaolinite migration. In contrast, the micro-fractures in well YS4 were not as developed as those in well YN4, thus leading to the accumulation of kaolinite to fill the primary and secondary pores in situ.

Table 7
The content of authigenic kaolinite in Lower Jurassic Ahe Formation sandstone, well YS4 and well YN4.

Well	Depth (m)	Authigenic kaolinite (%)	Well	Depth (m)	Authigenic kaolinite (%)	Well	Depth (m)	Authigenic kaolinite (%)
YS4	3980.59	1.2	YS4	4001.27	2.1	YS4	4101.24	1.3
YS4	3981.11	4.2	YS4	4003	4.96	YN4	4365	13.12
YS4	3982.11	2.86	YS4	4005.5	2.5	YN4	4374.46	1.98
YS4	3983.06	3	YS4	4006.78	5.92	YN4	4378.34	3.1
YS4	3984.06	1.8	YS4	4008.73	3.9	YN4	4379.86	0
YS4	3985.27	4.05	YS4	4041.12	0.07	YN4	4381.02	0
YS4	3987.8	3.74	YS4	4042.47	0	YN4	4382.1	4.86
YS4	3988.5	2.1	YS4	4044.06	0.88	YN4	4404.75	8.28
YS4	3989.48	3	YS4	4045.42	0.96	YN4	4407.91	6.9
YS4	3990.5	3.85	YS4	4047.03	1.65	YN4	4409.25	2.72
YS4	3991.65	5.22	YS4	4048.35	0.24	YN4	4410.31	1.87
YS4	3992.67	2.53	YS4	4067.63	1.95	YN4	4417.92	2.34
YS4	3995.08	4.29	YS4	4069.22	0.09	YN4	4420.9	1.5
YS4	3996.21	0.63	YS4	4070.49	0.11	YN4	4423.26	0.7
YS4	3997.25	2.08	YS4	4072.07	0.08	YN4	4452.06	0.72
YS4	3999.3	1.65	YS4	4073.11	1.62	YN4	4452.9–4649.36	0
YS4	4000.4	2.2	YS4	4074.2	1.87	YN4		

Vermicular and pseudohexagonal flaky kaolinite was extensively developed in the primary and secondary pores in well YS4 (Fig. 18F). A large number of well-formed kaolinite and the mineral contact relationship, the cementation period of kaolinite was later than that of quartz overgrowth. Therefore, the distance from the deep-rooted fault and lateral compression of the second-order faults affected the deep fluids participating in diagenesis.

6. Conclusions

The authigenic quartz cements were in the form of Qo, ranging from 1.07 to 8.73%, with an average of 3.86%. The outer edge of the quartz overgrowth had a regular shape with thickness, and the color of the quartz overgrowth was non-luminescent under CL. By comparing the content of siliceous material provided by the dissolution and siliceous material contained in authigenic quartz, the siliceous material from the feldspar dissolution was not sufficient, and an external source of siliceous material is required to explain the strong silica cement. A histogram of the homogenization temperature of aqueous inclusions in the quartz overgrowth in the Lower Jurassic Ahe Formation sandstones was concentrated in the interval from 120 °C to 170 °C, which was higher than the maximum burial temperature (100 °C) of the Ahe Formation. Moreover, the rare earth element Eu exhibited a slight negative abnormality in terms of Qo. Therefore, the deep fluid had a significant influence on diagenesis in the reservoirs near the deep-rooted fault.

The other strong cement type, calcite, was the dominant carbonate cement and well-developed in the Lower Jurassic Ahe Formation sandstone. The calcite was mainly cemented in the primary pores after quartz overgrowth cementation, and its content ranged from 0 to 8.92% with an average of 1.47%. Calcite cementation mainly exhibited dark orange luminescence under CL. The $\delta^{13}C_{VPDB}$ values in calcite were at a low negative interval, ranging from −11.70‰ to −2.50‰. The $^{87}Sr/^{86}Sr$ values varied from 0.71272 to 0.71976, all of which were higher than 0.710, indicating the influence of the crustal source. Eu showed a slight positive abnormality in terms of calcite. Several trace elements were enriched in calcite in the Lower Jurassic Ahe Formation sandstones, including Fe, Mn, Al, Ni, Cu, Zn, and Co. In addition, authigenic rutile is often associated with calcite agglomeration. In conclusion, the deep fluid participated in the cementation of authigenic quartz and calcite in the Lower Jurassic Ahe Formation sandstones near the deep-rooted fault.

The cementation characteristics in terms of the phase, type, and cathodoluminescence color of authigenic quartz and calcite far from the deep-rooted fault were quite different from those near the deep-rooted fault. Authigenic quartz occurred mainly as Qo and Qm. Qm was more developed around the periphery of the Qo and in secondary pores produced by feldspar dissolution. Qo exhibited brown luminescence; whereas Qm showed brown luminescence or was non-luminescent. Calcite developed in two phases, in which early calcite was mainly developed in intergranular pores, and late calcite was mostly developed in secondary dissolved pores. Early and late calcite showed bright yellow and dark orange luminescence, respectively.

Declaration of competing interest

The authors declare that they have no known competing financial interests or personal relationships that could have appeared to influence the work reported in this paper.

Data availability

Data will be made available on request.

Acknowledgments

This study was jointly supported by PetroChina Major Research Program on Deep Petroleum System in the Tarim Basin (No. ZD 2019-183-001-003) and the National Natural Science Foundation of China (Grant No. 41672124).

References

Allegre, C.J., Michard, G., 1973. Introduction to Geochemistry. Reidel Publishing Company, Boston, D, p. 69.

Anna, B., Susanne, G., Peter, K., 2009. Porosity-preserving chlorite cements in shallow-marine volcaniclastic sandstones: evidence from Cretaceous sandstones of the Sawan Gas field, Pakistan. AAPG (Am. Assoc. Pet. Geol.) Bull. 93 (5), 595–615.

Cai, J., Wang, L., Li, J., 2008. Mineralogical characteristics of rutile with different occurrences and genetic types and their research significance. Geol. Miner. Deposits 4, 531–538.

Chen, H., Yang, S., Dong, C., Zhu, G., Jia, C., Wei, G., Wang, Z., 1997. Study of geothermal events in the Tarim Basin. Sci. Bull. 10, 1096–1099.

Deines, P., 1992. Mantle Carbon: Concentration, Mode of Occurrence, and Isotopic Composition. Springer Berlin Heidelberg, pp. 133–146.

Duan, Z., Li, D., 2008. Coupled phase and aqueous species equilibrium of the H_2O-CO_2-NaCl-$CaCO_3$ system from 0 to 250 °C, 1 to 1 000 bar with NaCl concentrations up to saturation of halite. Geochem. Cosmochim. Acta 72 (20), 5128–5145.

Ehrenberg, S.N., 1993. Preservation of anomalous high porosity in deeply buried sandstones by grain-coating chlorite: examples from the Norwe. AAPG (Am. Assoc. Pet. Geol.) Bull. 77 (7), 1260–1286.

Frimmel, H.E., 2009. Trace element distribution in neo-proterozoic carbonates as palaeo-environmental indicator. Chem. Geol. 258, 338–353.

Gong, L., Zeng, L., Du, Y., et al., 2015. Influences of structural diagenesis on fracture effectiveness: a case study of the Cretaceous tight sandstone reservoirs of Kuga Foreland Basin. J. China Inst. Min. Technol. 44 (3), 514–519.

Guo, X., Liu, K., Jia, C., Song, Y., Zhao, M., Lu, X., 2016. Effects of early petroleum charge and overpressure preservation in the giant Kela-2 gas field, Kuqa depression, Tarim basin, northwest China. AAPG (Am. Assoc. Pet. Geol.) Bull. 100 (2), 191–212.

Hu, A., Shen, A., Pan, L., Wang, Y., Li, X., Wei, D., 2018. The role of binary isotopes in carbonate reservoir research. Nat. Gas Geosci. 29 (1), 17–27.

Huang, W., Wang, X., 2016. The fault activity and evolution characteristics of the Dibei-Yiqi Creek structural belt in the east of Kuqa. Sci. Technol. Bull. 32 (8), 28–30.

Jia, C., 1999. Structural characteristics and oil and gas accumulation regularity in Tarim Basin. Xinjing Pet. Geol. 20 (3), 177–183.

Jia, C., Li, Q., 2008. Petroleum geology of Kela-2, the most productive gas field in China. Mar. Petrol. Geol. 25 (4/5), 335–343.

Jiang, T., Sun, X., 2018. Development of Keshen ultra-deep and ultra-high pressure gas reservoirs in the Kuqa forel and basin, Tarim basin: understanding points and technical counter measures. Nat. Gas. Ind. 38 (6), 1–9 (in Chinese with English abstract).

Jiang, Z., Li, F., Yang, H., Li, Z., Liu, L., Chen, L., Du, Z., 2015. Development characteristics of fractures in Jurassic tight reservoir in Dibei area of Kuqa depression and its reservoir-controlling mode. Acta Pet. Sin. 36 (S2), 102–111.

Jin, Z., Zhu, D., Hu, W., Zhang, X., Wang, Y., Ya, X., 2006. Geological and geochemical signatures of hydmthermai activity and their influence on carbonate reservoir beds in the Tarim Basin. Acta Geologiea Sinica 80 (2), 245–253.

Lai, J., Wang, G., Chai, Y., Wu, Q., Zhang, X., Sun, Y., 2017. Deep burial diagenesis and resrevoir quality evolution of high-temperature, high-pressures and stones: examples from Lower Cretaceous Bashijiqike Formation in Keshen area, Kuqa depression, Tarim basin of China. AAPG (Am. Assoc. Pet. Geol.) Bull. 101 (6), 829–862.

Lawrence, M., Greig, A., Collerson, K., Kamber, B., 2006. Rare earth element and yttrium variability in south east queensland waterways. Aquat. Geochem. 12, 39–72.

Li, G., Meng, Y., Dong, Z., Tang, H., Luo, Y., Zhang, T., 2007. Mechanism and significance of microfracture generation by microwave heating in sandstone reservoirs. Petrol. Explor. Dev. 1, 93–97.

Li, X., Xiao, X., Tang, Y., et al., 2004. The generation and accumulation of natural gas from yanan 2 gas poolin Kuqa depression. English Sci. Bull. 49 (Suppl. 1), 107–114.

Li, Y., Jia, A., He, D., 2013. Control factors on the formation of effective reservoirs in tight sands: examples from Guangan and Sulige gasfields. Acta Pet. Sin. 34 (1), 71–82.

Li, Z., Song, W., Peng, S., et al., 2004. Mesozoic-cenozoic tectonic relationships between the Kuqa subbasin and tian Shan, northwest China: constraints from depositional records. Sediment. Geol. 172 (3/4), 223–249.

Li, Z., Guo, H., Wang, D., et al., 2005. Mesozoic-Cenozoic tectonic transition in Kuqa Depression Tianshan, northwest China: evidence from sandstone detrital and geochemical records. Sci. China (Series D: Earth Sci. 48 (9), 1387–1402.

Li, Z., Tan, X., Xue, W., Qiu, Y., Yong, Y., Liu, Z., 2015. Material source and precipitation mechanism of siliceous cements in clastic rocks. Petrol. Geol. Eng. 29 (2), 19, 24+ 145-146.

Liu, B., Zhang, J., 1992. Sedimentary Diagenesis. Beijing Science Press, pp. 24–25.

Liu, X., Fu, H., Li, Z., Huang, Y., 2011. Discovery of rutile and strontium rhodochrosite in changxing formation-feixianguan formation of northeast sichuan and its genesis interpretation. J. Chengdu Univ. Technol. (Sci. Technol. Ed.) 38 (3), 321–327.

Liu, Y., Wu, G., Hu, J., et al., 2004. Analyzing the characteristics of yinan-2 gas reservoir in kuche depression of talimu basin. Nat. Gas. Ind. 24 (7), 12–14.

Liu, Z., Lu, H., Jia, C., et al., 2001. Structures and hydrocarbon accumulation in Kuqa rejuvenated foreland basin. Oil Gas Geol. 22 (4), 297–303.

Long, H., Xiang, C., Niu, J., et al., 2014. Hydrothermal fluid flow and its influence on the hydrocarbon migration and accumulation along Binhai fault in Qikou Sag, Bohai Bay Basin. Acta Pet. Sin. 35 (4), 673–684.

Lu, H., Chen, C., Liu, Z., Jia, D., Wang, G., Jia, C., 2000. Tectonic features and genesis of the Kucha regenerated foreland retrograde zone. J. Petrol. 3, 18–24+108.

Lu, X., Zhao, M., Liu, K., Zhuo, Q., Fan, J., Yu, Z., Gong, Y., 2018. Forming condition and mechanism of highly effective deep tight sandstone gas reservoir in Kuqa foreland basin. Acta Pet. Sin. 39 (4), 365–378 (in Chinese with English abstract).

Lv, X., Yang, N., Xie, Q., Yang, H., 2005. Carbonate reservoirs transformed by deep fluid in Tazhong area. Oil Gas Geol. 26 (3), 284–289.

Lv, X., Yang, N., Zhou, X., Yang, H., Li, J., 2008. Influence of Ordovieian carbonate reservoir beds in Tarim Basin by faulting. Sci. China (Serial D). 51 (Suppl. 2), 53–60.

Milledge, H.J., Mendelssohn, M.J., Seal, M., 1983. Carbon isotopic variation in spectral type II diamond. Nature 303, 791–792.

Nan, J., Wang, S., Yao, W., Lu, Y., 2007. Study of micro-fractures in the long 6-8 extra-low permeability reservoir of the Yanchang Formation in the Longdong area of the Ordos Basin. Rocky Oil Gas Reservoirs 4, 40–44.

Pang, F., Tang, Y., Song, H., Tang, W., 2021. Analysis of the deformation and stress evolution of the Jurassic thrust structure in the eastern Kuqa foreland basin. Geol. Sci.Technol. Bull. 40 (5), 123–135.

Ramm, M., 1992. Porosity-depth trends in reservoir sandstones theoretical models related to Jurassic sandstones offshore Norway. Mar. Petrol. Geol. 9 (5), 553–567.

Rezaee, M.R., Tingate, P.R., 1997. Origin of quartz cement in thetrrawarra sandstone, southern Cooper Basin, south Australia. J. Sediment. Res. 67, 168–177.

Schmidt, V., McDonald, D.A., 1982. Secondary Reservoir Porosity during Sandstone Digenetic. Beijing Petroleum Industry Press, pp. 272–276.

Shang, X., Liu, L., Gao, X., Jiang, Z., Liu, G., 2012. Characteristics of oil and gas transport system and transport mode in Yiqi Creek structural belt in Kuqa Depression. J. Daqing Pet. Inst. 36 (1), 31–40+110+5+4.

Shou, J., Zhu, G., Zhang, H., et al., 2004. Characteristics and evaluation of Mesozoic and Cenozoic clastic reservoirs in oil and gas basins in north China. China Petrol. Exploration 9 (5), 31–39.

Su, A., Du, J., Chen, H., et al., 2016. Diagenetic fluid type and activity history of controlling the development of abnormal pore zone: taking the north margin of Baodao Sag, Qiongdongnan Basin as an example. Nat. Gas Geosci. 27 (10), 1837–1847.

Sun, J., Li, Y., Zhang, Z., et al., 2009. Magnetostratigraphic data on Neogene growth folding in the foreland basin of the southern Tianshan Mountains. Geology 37 (11), 1051–1054.

Surdam, R.C., Boese, S.W., Crossey, L.J., 1984. The chemistry of secondary porosity. AAPG Memoir 37 (2), 127–149.

Tang, Y., Yang, X., Xie, H., et al., 2021. Tight gas reservoir characteristics and exploration potential of jurassic Ahe Formation in Kuqa depression, Tarim Basin. China Petrol. Exploration 26 (4), 113–124.

Taylor, S.R., 1964. Trace element abundances and the chondritic Earth model. Geochem. Cosmochim. Acta 28 (12), 1989–1998.

Tian, J., Yang, H., Wu, C., Mo, T., Zhu, W., Shi, L., 2020. Discovery of well Bozi 9 and ultra-deep natural gas exploration potential in the Kelasu tectonic zone of the Tarim basin. Nat. Gas. Ind. 40 (1), 11~19 (in Chinesewith English abstract).

Trull, T., Nadeau, S., Pineau, F., Polvé, M., Javoy, M., 1993. C-he systematics in hotspot xenoliths: implications for mantle carbon contents and carbon recycling. Earth Planet Sci. Lett. 118, 43–64.

Turekian, K.K., Wedepohl, K.H., 1961. Distribution of elements in some major units of earth`s crust. Geol. Soc. Am. Bull. 72, 175–190.

Veizer, J., Ala, D., Azmy, K., et al., 1999. 87Sr/86Sr, δ13C and δ18O evolution of Phanerozoic seawater. Chem. Geol. 161 (1–3), 59–88.

Wang, B., Huang, Z., Ma, P., Pan, Z., Wang, L., 2009. Establishment of the division standard, basis and principle of structural units in the Tarim Basin. Geotectonics and Metallogenesis 33 (1), 86–93.

Wang, Q., Shi, J., Xue, L., et al., 1999. Characteristics of fluid-rock interaction in clastic reservoir controlled by evolution of diagenetic environment-taking the southwest depression of Tarim Basin as an example. Acta Sedimentol. Sin. 17 (4), 584–591.

Wang, Q., Zhang, R., Yang, X., Yu, C., Xu, Z., Zhou, L., Wang, K., Zhang, L., 2022. Major breakthrough and geological significance of tight sandstone gas exploration in Jurassic Ahe Formation in Dibei area, eastern Kuqa depression. Acta Pet. Sin. 43 (8), 1049–1064.

Wang, Z., Li, Y., Xie, H., Neng, Y., 2016. Geological understanding on the formation of large-scale ultra-deep oil-gas field in Kuqa foreland basin. China Petrol. Exploration 21 (1), 37–43 (in Chinese with English abstract).

Wang, Z., Long, H., 2010. Different hydrocarbon accumulation histories in the kelasu-yijikelike structural belt of the Kuqa foreland basin. Acta Geol. Sin. 84 (5), 1195–1208.

Wu, W., Song, Y., Zhuang, L., 2023. Trace elemental compositions of ore-related hydrothermal calcite for Mississippi Valley-type deposit: a case study of the Duocaima giant Pb-Zn deposit, Qinghai, China. Acta Petrol. Mineral. 42 (1), 47–70.

Young, G.M., 1999. Some aspects of the geochemistry, provenance and palaeoclimatology of the Torridonian of NW Scotland. J. Geol. Soc. 156, 1097–1111.

Zeng, L., 2004. Characteristics and petroleum geologic sign of himalayan orogeny in Kuqa foreland basin. Oil Gas Geol. 25 (2), 175–179.

Zeng, L., Wang, H., Gong, L., et al., 2010. Impacts of the tectonic stress field on natural gas migration and access: case study of the Kuqa Depression in the Tarim Basin, China. Mar. Petrol. Geol. 27 (7), 1616–1627.

Zhang, R., Yang, H., Wang, J., Shou, J., Zeng, Q., Liu, Q., 2014. The formation mechanism and exploration significance of ultra-deep, low-permeability and tight sandstone reservoirs in Kuqa depression, Tarim basin. Acta Pet. Sin. 35 (6), 1057 ~1069 (in Chinese with English abstract).

Zhang, T., Fang, X., Song, C., Erwin Appel, Wang Y., 2014. Cenozoic tectonic deformation and uplift of the South Tian Shan: implications from magnetostratigraphy and balanced cross-section restoration of the Kuqa depression. Tectonophysics: Int. J. Geotectonics Geol. Phys. Interior Earth 628, 172–187.

Zhang, Z., Lin, W., Wang, Q., 2003. Process structural evolution of kelasu-yiqikelike structural belt in Kuqa depression. Geotect. Metallogenia 27 (4), 327–336.

Zhao, Z., Bao, G., Qian, Z., 2018. Geochemical characteristics of C-O isotopes and REE in the hydrothermal calcite from the shuanglongquan Pb-Zn deposit, southern Guizhou, China. Acta Mineral. Sin. 38 (6), 627–636.

Zhu, D., Jin, Z., Hu, W., Zhang, X., 2008. Effects of deep fluid on carbonates reservoir in Tarim Basin. Geol. Rev. 54 (3), 348–354.

Zhu, D., Meng, Q., Jin, Z., Hu, W., 2012. Thermodynamic analysis of the dissolution-filling effect of CO_2-rich deep fluids on carbonate rocks. Geoscience 47 (1), 187–201.

Zhu, R., Guo, H., Gao, Z., et al., 2008. Relationships of diagenetic fluid evolution, reservoir physical properties and migration of oil and gas-a case of marine clastic reservoirs from upper Ordovician to carboniferous in west Manjiaer sag, Tarim. Acta Geol. Sin. 82 (6), 835–843.